

# Dislocation structures formation induced by thermal stress in additive manufacturing: multiscale crystal plasticity modeling of dislocation transport

Daijun Hu<sup>a</sup>, Nicolò Grilli<sup>b</sup>, Wentao Yan<sup>a,\*</sup>

<sup>a</sup>*Department of Mechanical Engineering, National University of Singapore, Singapore 117575, Singapore*

<sup>b</sup>*Department of Mechanical Engineering, University of Bristol, Queen's Building, BS8 1TR, Bristol, UK*

---

## Abstract

The motion of dislocations governs the plastic deformation of crystalline materials, which in turn determines the mechanical properties. The complex thermal history, large temperature gradients and high cooling rates during the process of additive manufacturing (AM) can induce high dislocation density and unique dislocation structures in the material. The origin of these dislocation structures and their stability during mechanical loading are debated. A novel temperature dependent continuum dislocation dynamics (CDD) model is developed, in which four state variables are used for each slip system representing the total dislocation density, edge and screw geometrically necessary dislocation densities and dislocation curvature. The CDD model is fully coupled with a finite strain crystal plasticity solver, which captures the plastic deformation induced by the dislocation motion. A hybrid continuous and discontinuous Galerkin formulation is developed to accurately reproduce the dynamics of highly discontinuous dislocation density fields that are typical of dislocation structures. A multiscale modeling approach is used, in which the thermally induced deformation in specific grains of a polycrystal is extracted from larger scale crystal plasticity simulations of the laser powder-bed fusion process, and is then used for single crystal scale dislocation dynamics simulations. Simulation results reveal the dynamics of dislocation structure formation in grains at different positions during laser scanning and cooling stages. The effect of the cyclic thermal stress during multi-layer AM fabrication is also investigated. The simulations provide a new perspective on the specific conditions that should be satisfied during AM process for the formation of stable dislocation structures.

### *Keywords:*

Dislocation dynamics, Additive manufacturing, Finite element method, Crystal plasticity, Thermal stress

---

\*Corresponding author

Email address: [mpeyanw@nus.edu.sg](mailto:mpeyanw@nus.edu.sg) (Wentao Yan)

## 1. Introduction

The motion of dislocations in metals, alloys and other crystalline materials is one of the most important phenomena leading to plastic deformation of mechanical components and internal residual stresses, which can cause unexpected failures [1]. Controlling the dislocation structure formation during material processing and deformation is desirable to improve the strength of the metallic materials [2, 3, 4]. Researchers have been able to control dislocation structures by engineering grain boundaries or second-phase particles [2, 5]. The dislocation structures observed in the experiments can originate both from the manufacturing process and from complex loading paths. In order to manipulate the dislocation behavior, it is critical to understand how the dislocation structures are generated and how they evolve during the manufacturing process. This would shed light in novel strategies to improve the mechanical properties.

Additive manufacturing (AM) is a promising technology that can fabricate complex structures from digital files. Laser powder-bed-fusion (L-PBF) is a commonly used metallic AM technology, and can flexibly adjust a wide range of process parameters, which has great potential to tailor the performance of metal parts [6, 7]. In L-PBF process, powder particles are fused by a high-energy laser beam which forms a molten pool, together with large temperature gradients, high cooling rates and complex thermal history during the heating-cooling cycles [8, 9, 10]. All these factors contribute to the unique microstructures and dislocation networks that are different from traditional manufacturing. They lead to extraordinary mechanical properties, such as high strength and ductility [7, 11, 12, 13]. Recent experiments show that the dislocation network in AM metals can hinder dislocation motion and increase the accumulated dislocation density resulting in high strength [14]. However, under high stress, hindered dislocations are still able to transmit through the dislocation walls to ensure a stable plastic flow [15]. Dislocation structures may be responsible for the activation of other deformation phenomena, such as twinning in AM stainless steel (SS) [16], which would otherwise not be a dominant mechanism. Dislocation structures are also correlated with fracture because crack surfaces have been detected on the walls with high-density cellular dislocation structures [17]. Therefore, AM techniques offer the opportunity to design and fabricate high-performance metallic materials by adjusting the process parameters to obtain unique dislocation structures. Because of this attractive prospect, it is of utmost importance to have a deeper understanding of the underlying mechanisms, such as the nucleation, growth and evolution of dislocation structures during the AM process [18, 19]. Previously, dislocation structures have been studied in the context of cyclic fatigue [20, 21, 22, 23, 24] and stage III of work hardening [25, 26]. The possibility that thermal stress can induce dislocation structures has not been widely investigated. Recent advances in AM techniques [14, 15, 7] have stimulated new research about thermo-mechanical theories of the dislocation motion in heterogeneous temperature fields with large temperature gradients [27]. Previous simulations suggested that chemical segregation may have a role in the dislocation structures formation in AM metals [28]. However, experiments on copper [18] show that high purity metals also have this phenomenon. Therefore, the formation of dislocation structures in AM metals still remains a debated issue.

During AM processes, dislocation motion takes place due to thermal stress that is caused by the highly inhomogeneous temperature field [1, 14]. The experimental analysis of the dislocation dynamics during the AM process is extremely difficult. Dislocations can be observed using microscopy methods, such as transmission electron microscopy (TEM) [29] and scanning electron microscopy (SEM) [30]. However, only the final dislocation structures after manufacturing can be observed, while the observation area and depth are limited. Dislocation structures may also be altered or even restructured during sample preparation before observation. Moreover, in-situ electron microscopy techniques cannot be easily used on samples subjected to laser beams during L-PBF process, thus there is no intuitive experimental report on the formation of dislocation structures during the fabrication process. In-situ synchrotron X-ray diffraction has overcome these difficulties [31], but individual dislocation structures could not be resolved. Modeling is a promising approach and has been previously employed to understand the relationship between mechanical properties and dislocation structures [32, 33]. Many different dislocation-based models have been proposed to investigate a large variety of interesting phenomena [34, 35, 36, 37]. Due to the discrete nature of dislocation lines, computational methods such as molecular dynamics and discrete dislocation dynamics (DDD) have been commonly used [38, 39, 40, 41]. However, high computational cost and limited time frame are required for the discrete formulations. Continuum dislocation dynamics (CDD) models, which can be easily implemented in existing finite element software and used with arbitrary boundary conditions, have also been developed to cope with these issues [42, 43, 44, 45]. Since the curvature of dislocations is an important variable to reproduce dislocation cells in AM parts, the higher dimensional CDD model is appropriate for this work and it has great potential for introducing complex dislocation mechanisms [46, 47, 48]. However, there are very few studies on modeling the dislocation dynamics during the AM processes. Currently, there are still some critical problems to be addressed:

- What is the origin of the high-density dislocation structures in AM metals?
- Is thermal stress in AM process sufficient for the formation of high-density dislocation structure?
- Are the dislocation structures in AMed materials becoming stable during the process or under further loading?
- Are the dislocation structures forming only inside specific grains at specific positions in the sample?
- What is the effect of the temperature field during multi-layer AM fabrication on the dislocation evolution?

In this work, multiscale models including a polycrystal model and a small scale temperature dependent CDD model are developed to answer the questions above. [49, 50, 51], The CDD approach developed by Hochrainer et al. [47, 48] is used and extended in this work, which is able to model the accumulation and structure formation of the curved dislocations [19, 52]. The capability of this model to describe comprehensively the dislocation motion and reproduce dislocation patterning was demonstrated by Sandfeld et al. [53, 54, 55], but

their studies were carried out using simplified load conditions at room temperature, and some dislocation mechanisms, such as annihilation, were not taken into account. The numerical scheme used for the present CDD model is a hybrid continuous and discontinuous Galerkin formulation, which is a modification of the one proposed by Schulz et al. [52]. The uniqueness of this approach lies in the decomposition of the dislocation density into positive/negative and edge/screw components to calculate the interface fluxes. Moreover, this approach can describe highly discontinuous dislocation density fields, e.g. dislocation dipoles. The developed dislocation model is fully coupled with a finite strain crystal plasticity solver, and is able to capture arbitrarily oriented slip systems. This is an advance over previous works based on the higher dimensional CDD models that were limited to small strain formulations [52, 50].

To address the dislocation dynamics in AM process, it is necessary to capture the realistic information in AM process, including thermal deformation and temperature history that affect the temperature dependent dislocation kinetics. Modeling L-PBF process is challenging because of the inhomogeneous temperature fields and complex thermal strain history. This challenge is addressed by using the multiscale approach in which the temperature field is extracted from thermal fluid flow simulations and is then incorporated into the crystal plasticity finite element method (CPFEM) to accurately determine the thermal strain as a function of time in individual grains [56, 57]. The thermal deformation and temperature history from polycrystal simulations are introduced into the small scale 3D CDD simulations for the dislocation dynamics. The dislocation evolutions in single-layer AM process, as well as in multi-layer fabrication, are simulated to investigate the formation and stabilization of dislocation structures.

## 2. Material model and multiscale framework

A dislocation-based thermal-mechanical crystal plasticity model is used in this work, which is fully coupled with a CDD formulation. The finite strain crystal plasticity framework is introduced in Section 2.1. The CDD model is used to account for the dislocation density evolution as detailed in Section 2.2. A hybrid continuous and discontinuous Galerkin formulation is used for the numerical implementation. The 3D displacement vector  $\mathbf{u}$  is the first variable that the finite element solver calculates based on the stress equilibrium equation  $\nabla \cdot \boldsymbol{\sigma} = 0$ , where  $\boldsymbol{\sigma}$  is the Cauchy stress. This part of the coupled problem is solved with the standard continuous Galerkin method. The CDD equations include four more variables for each slip system and can reproduce dislocation fluxes. These four additional variables are solved with the discontinuous Galerkin method, as detailed in section 2.3. The dislocation annihilation mechanism is also implemented in this framework as described in Section 2.4. The multiscale framework for L-PBF process and grain extraction strategy for this work are described in Section 2.5 and 2.6, respectively. All the above models are implemented in the finite element framework MOOSE [58].

### 2.1. Kinetics model

The deformation gradient  $\mathbf{F}$  can be decomposed into thermal-elastic and plastic parts [59, 60, 61]:

$$\mathbf{F} = \mathbf{F}_e \mathbf{F}_p, \quad (1)$$

where  $\mathbf{F}_e$  is the thermal-elastic part and  $\mathbf{F}_p$  is the plastic part, which takes the plastic slip on all slip systems in the crystal into account as [62, 63]:

$$\mathbf{L}_p = \dot{\mathbf{F}}_p \mathbf{F}_p^{-1} = \sum_{\alpha=1}^{N_s} \dot{\gamma}^\alpha \mathbf{m}^\alpha \otimes \mathbf{n}^\alpha, \quad (2)$$

where the vectors  $\mathbf{m}^\alpha$  and  $\mathbf{n}^\alpha$  are unit vectors representing the slip direction vectors and normal vectors of slip system  $\alpha$ , respectively.  $N_s$  is the number of slip systems and  $\mathbf{L}_p$  is the so-called plastic velocity gradient. The stress-dependent plastic slip rates on the slip systems  $\dot{\gamma}^\alpha$  are determined by the Orowan's law [64]:

$$\dot{\gamma}^\alpha = \rho_t^\alpha v^\alpha b^\alpha, \quad (3)$$

where  $\rho_t^\alpha$  is the total dislocation density on slip system  $\alpha$ ,  $\mathbf{b}^\alpha$  is the Burgers vector and  $v^\alpha$  is the dislocation velocity determined by [25]:

$$\mathbf{v}^\alpha = \begin{cases} B(|\tau^\alpha| - \tau_c^\alpha) \operatorname{sign}(\tau^\alpha) \mathbf{m}^\alpha & \text{if } |\tau^\alpha| > \tau_c^\alpha \\ 0 & \text{otherwise} \end{cases} \quad (4)$$

where  $\tau^\alpha$  is the resolved shear stress (RSS) on slip system  $\alpha$  and  $B$  is the dislocation mobility. The relationship between dislocation velocity and  $\tau^\alpha$  is linear and the phonon wind is not considered because the dislocation velocity in the following simulations is relatively low [65]. The dislocation mobility has been found to be temperature dependent for stainless steels [66] but its tiny effect on the dislocation velocity is not taken into account in this work. To avoid numerical divergence, a maximum absolute value of the dislocation velocity  $v_{max}$  is set in our model, which is sufficient to accommodate the plastic deformation while keeping the RSS close to  $\tau_c^\alpha$  in the plastic regime.  $\tau_c^\alpha$  is the critical resolved shear stress (CRSS), which is given by a Taylor hardening equation considering bow-out effect [1, 67, 68]:

$$\tau_c^\alpha = \alpha_r G b^\alpha \sqrt{\rho_t^\alpha} + \alpha_b G b^\alpha / R^\alpha, \quad (5)$$

where  $G$  is the shear modulus,  $\alpha_r$  is the dislocation resistance coefficient [69, 70],  $\alpha_b$  is the coefficient of the bow-out stress, and  $R^\alpha$  is the average radius of curved dislocations given by  $R^\alpha = \rho_t^\alpha / q_t^\alpha$  [1, 55], where  $q_t^\alpha$  is the total curvature density of the dislocation lines.

Taking the temperature dependence of the CRSS into account, the CRSS at temperature  $T$  can be described by an exponential function calibrated using experimental data of 316L stainless steel (SS) [71]:

$$\tau_c^\alpha(T) = (k_A + k_B \cdot \exp[-k_C(T - T_0)]) \cdot \tau_c^\alpha(T_0), \quad (6)$$

where  $T_0$  is the reference temperature, and  $k_A$ ,  $k_B$  and  $k_C$  are constants obtained by calibration. The thermal and elastic deformation gradient can be used to calculate the Green-

Lagrange strain tensor as:

$$\mathbf{E}_e = \frac{1}{2}(\mathbf{F}_e^T \mathbf{F}_e - \mathbf{I}) , \quad (7)$$

where  $\mathbf{I}$  is the identity matrix. The second Piola-Kirchhoff stress used to calculate the stress equilibrium is given by:

$$\mathbf{S} = \mathbb{C}(\mathbf{E}_e - \boldsymbol{\alpha}) , \quad (8)$$

where  $\boldsymbol{\alpha}$  is the thermal eigenstrain calculated by the temperature change and a temperature-dependent volumetric thermal expansion coefficient [56, 72].  $\mathbb{C}$  is the elasticity tensor of 316L SS. The temperature dependence of the elasticity tensor can be approximated by a linear function [71]:

$$\mathbb{C}_{ij}(T) = \mathbb{C}_{ij}(T_0) + \frac{d\mathbb{C}_{ij}}{dT}(T - T_0) , \quad (9)$$

which is used to describe the elasticity tensor of the material in solid state.

## 2.2. Dislocation density evolution equations

The CDD model includes four state variables for each slip system  $\alpha$  [48]: the total dislocation density  $\rho_t^\alpha$ , the edge and screw contributions to the geometrically necessary dislocation (GND) density  $\rho_e^\alpha$  and  $\rho_s^\alpha$  [73], and the total curvature density  $q_t^\alpha$ . Given an infinitesimal area  $dS$ ,  $q_t^\alpha$  is the sum of the local curvatures of all the dislocation lines crossing that area. For instance, a set of dislocation loops with radius  $R$  and area density  $\rho_t$  has curvature density  $q_t = \rho_t/R$ . In the following,  $x$  and  $y$  denote the coordinates in the slip system reference frame:  $x$  is the slip direction,  $z$  is the slip plane normal, thus  $x$ ,  $y$  and  $z$  form a right-handed coordinate system. The superscript  $\alpha$  that indicates the specific slip system will be dropped in the rest of this article to simplify the notation. The evolution equations shown in the following hold for each slip system independently:

$$\frac{\partial \rho_t}{\partial t} = -\frac{\partial (\rho_e v)}{\partial x} - \frac{\partial (\rho_s v)}{\partial y} + \dot{\rho}_{\text{ann}} + v q_t , \quad (10)$$

$$\frac{\partial \rho_e}{\partial t} = -\frac{\partial (\rho_t v)}{\partial x} , \quad (11)$$

$$\frac{\partial \rho_s}{\partial t} = -\frac{\partial (\rho_t v)}{\partial y} , \quad (12)$$

$$\begin{aligned} \frac{\partial q_t}{\partial t} = & -\frac{\partial}{\partial x} \left( \frac{v \rho_e q_t}{\rho_t} \right) - \frac{\partial}{\partial y} \left( \frac{v \rho_s q_t}{\rho_t} \right) - \frac{\partial}{\partial x} \left( \frac{\rho_t \partial v}{2 \partial x} \right) - \frac{\partial}{\partial y} \left( \frac{\rho_t \partial v}{2 \partial y} \right) \\ & - \frac{\partial}{\partial x} \left[ \frac{(\rho_s^2 - \rho_e^2)}{2\sqrt{\rho_e^2 + \rho_s^2}} \frac{\partial v}{\partial x} - \frac{\rho_e \rho_s}{\sqrt{\rho_e^2 + \rho_s^2}} \frac{\partial v}{\partial y} \right] \\ & - \frac{\partial}{\partial y} \left[ -\frac{\rho_e \rho_s}{\sqrt{\rho_e^2 + \rho_s^2}} \frac{\partial v}{\partial x} + \frac{(\rho_e^2 - \rho_s^2)}{2\sqrt{\rho_e^2 + \rho_s^2}} \frac{\partial v}{\partial y} \right] . \end{aligned} \quad (13)$$

The dislocation multiplication is implemented by the last term in equation (10), which describes the increase of dislocation line length caused by the curved dislocation evolution, including the Frank-Read source [55, 49, 74]. The gradient terms represent the transport of dislocations and curvature density. This system of equations for the four state variables is a second order multipole expansion of the Kröner-Nye tensor in the angle  $\theta$  that a dislocation line forms with the  $x$  axis [75]. After estimation of the dislocation climb rate in the AM temperature range [76, 77, 78], it has been established that the jog movement does not exceed 10% of the dislocation velocity even at the maximum value and is almost negligible as the rapid cooling progresses, so it is not considered in this work.

### 2.3. CDD numerical implementation

The numerical scheme used to calculate the variables of the CDD model is a discontinuous Galerkin formulation with implicit time integration, which is a modification of the one proposed by Schulz et al. [52]. The novel idea of the present approach is to decompose the dislocation density into positive/negative and edge/screw components to calculate the interface fluxes. These components should not be confused with the variables  $\rho_e$  and  $\rho_s$ , which represent the edge and screw contributions of the GND density. The specific definition is explained in this section and the novelty of this approach is the ability to describe highly discontinuous dislocation density fields, such as dislocation dipoles, as shown by the test cases in the following.

These equations are converted by the solver into their weak forms, in which the sum over all elements  $E$  with volume  $\Omega_E$  is taken. For instance, the weak form of equation (10), neglecting  $\dot{\rho}_{\text{ann}}$ , can be written as:

$$\sum_E \int_{\Omega_E} \frac{\partial \rho_t}{\partial t} \Psi \, dV = - \sum_F \int_{\partial \Omega_F} \begin{pmatrix} \rho_e v \\ \rho_s v \end{pmatrix} \cdot \hat{\mathbf{n}} \Psi \, dS + \sum_E \left( \int_{\Omega_E} \begin{pmatrix} \rho_e v \\ \rho_s v \end{pmatrix} \cdot \nabla \Psi \, dV + \int_{\Omega_E} v q_t \Psi \, dV \right) , \quad (14)$$

in which the divergence theorem is applied to the advection term and the gradient  $\nabla = (\partial/\partial x, \partial/\partial y)$  is introduced. A sum over all interfaces  $F$  is taken.  $\Psi$  is an arbitrary test function. The surface term, which is the first term on the right-hand side of equation (14), represents the boundary conditions when the surface  $\partial \Omega_F$  corresponds to the boundary. If  $\partial \Omega_F$  is a boundary between two elements, called inner boundary, this surface advection term is not uniquely defined because the variables  $\rho_e$  and  $\rho_s$  are discontinuous at the boundary  $\partial \Omega_F$ . In the current model we choose a surface advection term that depends on positive and negative, edge and screw, dislocation densities. First, for each inner boundary, a flux term  $\mathbf{F}_{\partial \Omega_F}$  is defined as:

$$- \int_{\partial \Omega_F} \begin{pmatrix} \rho_e v \\ \rho_s v \end{pmatrix} \cdot \hat{\mathbf{n}} \Psi \, dS = - \mathbf{F}_{\partial \Omega_F} \cdot \hat{\mathbf{n}} . \quad (15)$$

Each inner boundary  $\partial \Omega_F$  separates an element with volume  $\Omega_E$  from an element with volume  $\Omega_N$ , where the subscript  $N$  means neighbouring element. Each inner boundary  $\partial \Omega_F$  appears only once in the sum in the first term of the right-hand side of equation (14). The

unit normal vector  $\hat{\mathbf{n}}$  is perpendicular to the interface and points from  $\Omega_E$  towards  $\Omega_N$ . The variables  $\rho_e$  and  $\rho_s$  are discontinuous at the interface  $\partial\Omega_F$  and take different values at the inner interface in  $\Omega_E$ , called  $\rho_e|_{\partial\Omega_E}$  and  $\rho_s|_{\partial\Omega_E}$ , and at the outer interface in  $\Omega_N$ , called  $\rho_e|_{\partial\Omega_N}$  and  $\rho_s|_{\partial\Omega_N}$ . Therefore,  $(\rho_e|_{\partial\Omega_E} - \rho_e|_{\partial\Omega_N})$  and  $(\rho_s|_{\partial\Omega_E} - \rho_s|_{\partial\Omega_N})$  are the variable jumps at the interface  $\partial\Omega_F$ . Edge and screw, positive and negative dislocation densities are defined as:

$$\rho_e^+ = \frac{1}{2} \left( \sqrt{\rho_t^2 - \rho_s^2} + \rho_e \right) , \quad (16)$$

$$\rho_e^- = \frac{1}{2} \left( \sqrt{\rho_t^2 - \rho_s^2} - \rho_e \right) , \quad (17)$$

$$\rho_s^+ = \frac{1}{2} \left( \sqrt{\rho_t^2 - \rho_e^2} + \rho_s \right) , \quad (18)$$

$$\rho_s^- = \frac{1}{2} \left( \sqrt{\rho_t^2 - \rho_e^2} - \rho_s \right) . \quad (19)$$

Let  $\rho_e^+|_{\partial\Omega_E}$ ,  $\rho_e^-|_{\partial\Omega_E}$ ,  $\rho_s^+|_{\partial\Omega_E}$ ,  $\rho_s^-|_{\partial\Omega_E}$  be the quantities in equations (16)-(19) calculated at the inner interface in  $\Omega_E$ , while  $\rho_e^+|_{\partial\Omega_N}$ ,  $\rho_e^-|_{\partial\Omega_N}$ ,  $\rho_s^+|_{\partial\Omega_N}$ ,  $\rho_s^-|_{\partial\Omega_N}$  are those calculated at the outer interface in  $\Omega_N$ . The flux is defined as the sum of two contributions from the inner and outer interfaces:

$$\mathbf{F}_{\partial\Omega_F} = \mathbf{F}_{\partial\Omega_E} + \mathbf{F}_{\partial\Omega_N} , \quad (20)$$

where:

$$\mathbf{F}_{\partial\Omega_E} = \begin{pmatrix} v(\rho_e^+|_{\partial\Omega_E} - \rho_e^-|_{\partial\Omega_N}) \Psi_{\partial\Omega_E} H(v\hat{n}_x) \\ v(\rho_s^+|_{\partial\Omega_E} - \rho_s^-|_{\partial\Omega_N}) \Psi_{\partial\Omega_E} H(v\hat{n}_y) \end{pmatrix} + \begin{pmatrix} v(\rho_e^+|_{\partial\Omega_N} - \rho_e^-|_{\partial\Omega_E}) \Psi_{\partial\Omega_E} H(-v\hat{n}_x) \\ v(\rho_s^+|_{\partial\Omega_N} - \rho_s^-|_{\partial\Omega_E}) \Psi_{\partial\Omega_E} H(-v\hat{n}_y) \end{pmatrix} \quad (21)$$

$$\mathbf{F}_{\partial\Omega_N} = - \begin{pmatrix} v(\rho_e^+|_{\partial\Omega_E} - \rho_e^-|_{\partial\Omega_N}) \Psi_{\partial\Omega_N} H(v\hat{n}_x) \\ v(\rho_s^+|_{\partial\Omega_E} - \rho_s^-|_{\partial\Omega_N}) \Psi_{\partial\Omega_N} H(v\hat{n}_y) \end{pmatrix} - \begin{pmatrix} v(\rho_e^+|_{\partial\Omega_N} - \rho_e^-|_{\partial\Omega_E}) \Psi_{\partial\Omega_N} H(-v\hat{n}_x) \\ v(\rho_s^+|_{\partial\Omega_N} - \rho_s^-|_{\partial\Omega_E}) \Psi_{\partial\Omega_N} H(-v\hat{n}_y) \end{pmatrix} \quad (22)$$

where  $H$  is the Heaviside function,  $\Psi_{\partial\Omega_E}$  and  $\Psi_{\partial\Omega_N}$  are the test functions calculated at the inner interface in  $\Omega_E$  and at the outer interface in  $\Omega_N$  respectively. The Heaviside function selects one of the two terms in the two components of the vector  $\mathbf{F}_{\partial\Omega_F}$  depending on the signs of  $v\hat{n}_x$  and  $v\hat{n}_y$ . This selection represents the flux directions and it is typical of upwind schemes [62]. The two terms  $\mathbf{F}_{\partial\Omega_E}$  and  $\mathbf{F}_{\partial\Omega_N}$  are proportional to  $\Psi_{\partial\Omega_E}$  and  $\Psi_{\partial\Omega_N}$  respectively, which indicates that they contribute to the residuals of the element  $\Omega_E$  and of the neighbouring element  $\Omega_N$  respectively. The minus sign in equation (22) ensures that the residual term in equation (15) is conservative, i.e. the total dislocation density exiting the element  $\Omega_E$  enters the element  $\Omega_N$  and vice versa.

The motivation behind equations (20)-(22) is schematically shown in Fig. 1. Suppose a total dislocation density  $\rho_t$  and an edge GND density  $\rho_e$  is present. The interface between two elements with volumes  $\Omega_E$  and  $\Omega_N$  is supposed to be perpendicular to the edge dislocation velocity  $\vec{v}$ , pointing towards the right direction, which is the positive  $x$  direction. In this condition, positive edge dislocations  $\rho_e^+$  will move towards the right, while negative edge dislocations  $\rho_e^-$  will move towards the left. This is represented by the first term on the right-hand side of equations (21)-(22).

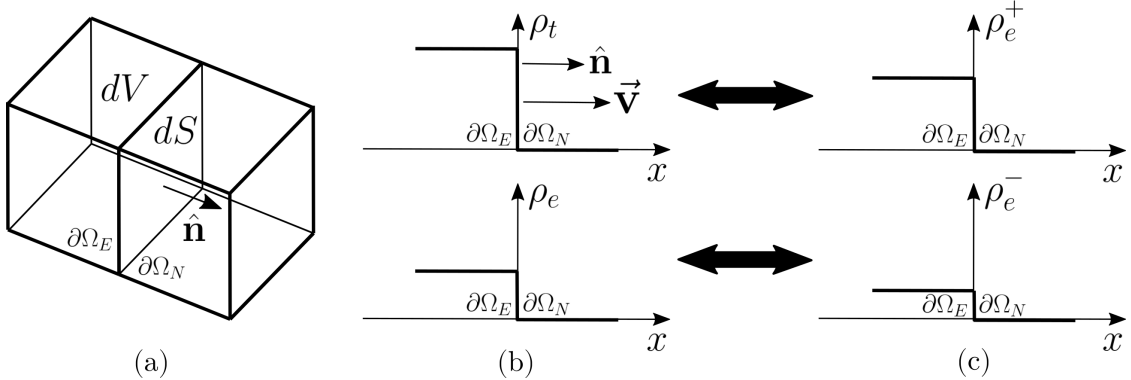


Figure 1: Graphical representation of the flux terms in equations (20)-(22).

The weak form of the other evolution equations for the dislocation density is reported in [Appendix A](#), where the choice of the corresponding fluxes is also explained. On external boundaries, we use periodic boundary conditions for the dislocation fluxes. The Galerkin method is used, in which the test functions  $\Psi$  are the same as the shape functions that are used to interpolate the variables. In addition, very small diffusion terms are added to equations (10)-(13) for numerical stabilization, as previously proposed by Sandfeld and Zaiser [55]. Specifically, four terms  $D\nabla^2\rho_t$ ,  $D\nabla^2\rho_e$ ,  $D\nabla^2\rho_s$ ,  $D\nabla^2q_t$  are added to the right-hand side of equations (10), (11), (12) and (13) respectively. The artificial diffusion coefficient is chosen as  $D = 0.001 \mu\text{m}^2/\mu\text{s}$ , which is small enough to avoid numerical fluctuations and to provide good simulation convergence without affecting the solution significantly. This is because the total time of the reference simulation presented in Section 3.1 is about  $t = 3500 \mu\text{s}$  and the characteristic diffusion length is of the order of  $\sqrt{Dt}$ . This distance is comparable with the element size and it is much shorter than the distance that dislocations travel due to stress-driven transport.

A straight dislocation line test case is carried out on a plane geometry to show the capabilities of the novel numerical scheme. Specifically, the possibility to handle highly discontinuous dislocation density field is highlighted. A pure edge dislocation line is initially set in the middle of the geometry, perpendicular to  $x$  direction, as shown in Fig. 2(a)-(c), which contains positive part in red and negative part in blue as shown in Fig. 2(d). This particular configuration represents an edge dislocation dipole and the field  $\rho_e$  has a discontinuity in the center of the geometry, changing from positive to negative at the interface between the elements. Given a pure shear load, it can be observed that the positive part moves along the shear direction and the negative part moves oppositely, revealing that

the appropriate dislocation evolution is achieved and the capability of the model to handle this discontinuous dislocation configuration. To avoid repetitions, the similar results of the screw dislocation test case are not shown here. In addition, the loop expansion test case for dislocation curvature evolution is reported in [Appendix B](#).

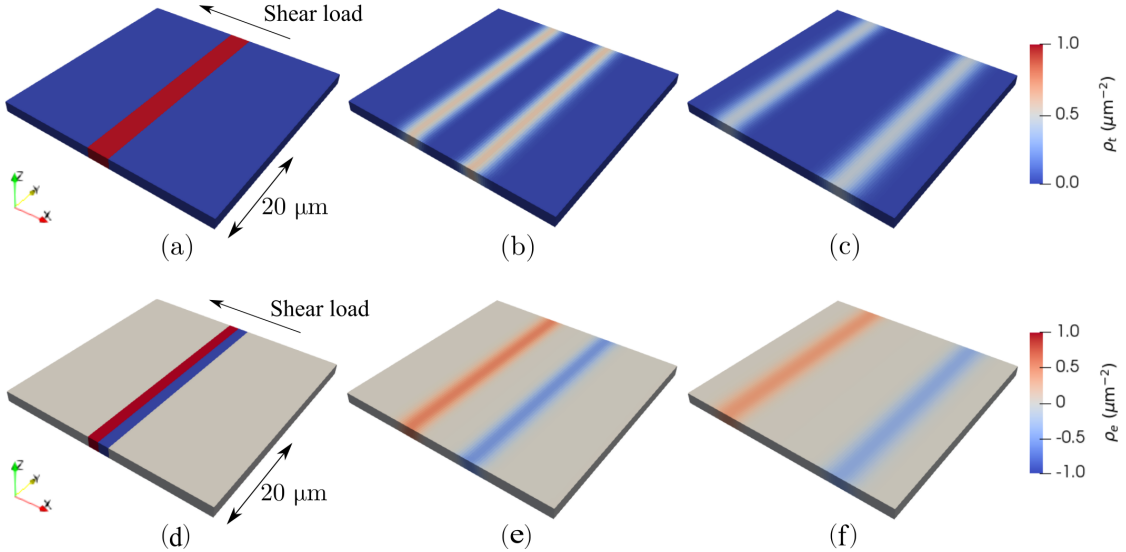


Figure 2: Test case with an edge dislocation dipole: total dislocation density  $\rho_t$  at (a)  $t = 0$ , (b)  $t = 13 \mu\text{s}$ , (c)  $t = 26 \mu\text{s}$  and edge GND density  $\rho_e$  at (d)  $t = 0$ , (e)  $t = 13 \mu\text{s}$ , (f)  $t = 26 \mu\text{s}$ .

#### 2.4. Implementation of dislocation annihilation

The dislocation annihilation law is used to describe the annihilation of opposite signed dislocations when the distance between two dislocation lines is lower than a characteristic length  $\check{d}_c$  [79]. The purpose of introducing this term is to understand how the reduction of the total dislocation density can change the features of dislocation structures, especially in regards to the ratio between high and low dislocation density regions. Therefore, the annihilation rate is approximated as:

$$\dot{\rho}_{\text{ann}} = -4\check{d}_c\rho_t^2 |v| . \quad (23)$$

It is proportional to the absolute value of the dislocation velocity  $v$  and to the square of  $\rho_t$  because it models the close encounters of dislocations moving along opposite directions. Since the annihilation mechanisms of edge and screw dislocations are different [80, 81], the annihilation distances of edge and screw dislocations in 316L SS are different, i.e. 1.3 nm and 50 nm respectively [82, 83]. As the unique annihilation distance  $\check{d}_c$  is used in the present work, an intermediate characteristic length is used for annihilation. In [Section 3.2](#), a series of simulations with different annihilation distances are carried out to investigate the effect of the  $\check{d}_c$  on the dislocation structures.

All the model and material parameters involved in this work are listed in the [Table 1](#).

Table 1: Model and material parameters used in the simulations [71, 72, 23, 84, 25, 67, 85, 56]

Burgers vector ( $\mathbf{b}^\alpha$ )	0.258 nm
Number of slip system ( $N_s$ )	12
Dislocation mobility ( $B$ )	0.04 $\mu\text{m}/(\mu\text{s}\cdot\text{MPa})$
Shear modulus ( $G$ )	86 GPa
Dislocation resistance coefficient ( $\alpha_r$ )	0.4
Bow-out effect coefficient ( $\alpha_b$ )	0.5
Maximum dislocation velocity ( $v_{max}$ )	0.04 $\mu\text{m}/\mu\text{s}$
Reference temperature ( $T_0$ )	298 K
Temperature dependence of CRSS ( $k_A$ )	0.53
Temperature dependence of CRSS ( $k_B$ )	0.47
Temperature dependence of CRSS ( $k_C$ )	0.008
Elastic constants at $T = T_0$ ( $C_{11}$ )	204.6 GPa
Elastic constants at $T = T_0$ ( $C_{12}$ )	137.7 GPa
Elastic constants at $T = T_0$ ( $C_{44}$ )	126.2 GPa
Derivative of elastic constant ( $dC_{11}/dT$ )	-90.33 MPa/K
Derivative of elastic constant ( $dC_{12}/dT$ )	-45.10 MPa/K
Derivative of elastic constant ( $dC_{44}/dT$ )	-51.78 MPa/K
Dislocation annihilation characteristic distance ( $\check{d}_c$ )	1.3 nm/12.8 nm/25 nm

## 2.5. Multiscale model of the L-PBF process

A multiscale computational framework, as shown in Fig. 3, is adopted to simulate the L-PBF process, including a thermal-fluid flow model, a phase field model for grain growth and a phenomenological CPFEM [56]. The purpose is to accurately determine the deformation field at the grain length scale that will be subsequently used for the CDD model simulation. To reach this target, the temperature field is obtained from thermal-fluid flow simulations incorporating many physical factors, including the ray-tracing heat source model for laser, thermal conduction, surface radiation and convection, latent heat, evaporation, recoil pressure, viscosity, buoyancy force, surface tension and Marangoni effect [86, 87]. The grain structure is obtained from a phase field model for grain growth, in which the grain nucleation and growth, competitive growth, grain coarsening and other phenomena are taken into account [88]. The simulation domain in CPFEM simulations represents the last deposited layer on the top of the sample and also includes part of the substrate that does not melt, representing previously deposited layers.

The process parameters are taken from the experimental work by Wang et al.[7] on AM 316L SS. The temperature profiles from thermal-fluid flow simulations are introduced into the CPFEM simulations, in which the melting and solidification are described using the residual stiffness method [89]. The grain structure predicted by the phase field model is input into the CPFEM model to reproduce the morphology of grains that is typical of AM 316L SS. The Euler angles that characterize grain orientation are extracted from Electron BackScatter Diffraction (EBSD) experiments on the same material [85]. The CPFEM employed for the

L-PBF process simulation is based on phenomenological power-law flow rules. The previous works mainly focused on the deformation at the grain length scale [57, 90], leading to a better understanding of the mechanisms of residual deformation and process-structure-property relationship in AM process. It has been calibrated by comparing the simulated lattice strain inside specifically oriented grain families with the one measured by X-Ray diffraction measurements [57]. This guarantees that the deformation history at the grain length scale is determined with good accuracy. This information is used to set boundary conditions for the 3D CDD model, as explained in Section 2.6. The temperature history of each grain is also necessary for the temperature-dependent CDD model. More details about the multiscale modeling framework and phenomenological CPFEM are reported in our previous works [56, 57], while in the present paper the previous results are utilized as inputs for the CDD model simulations.

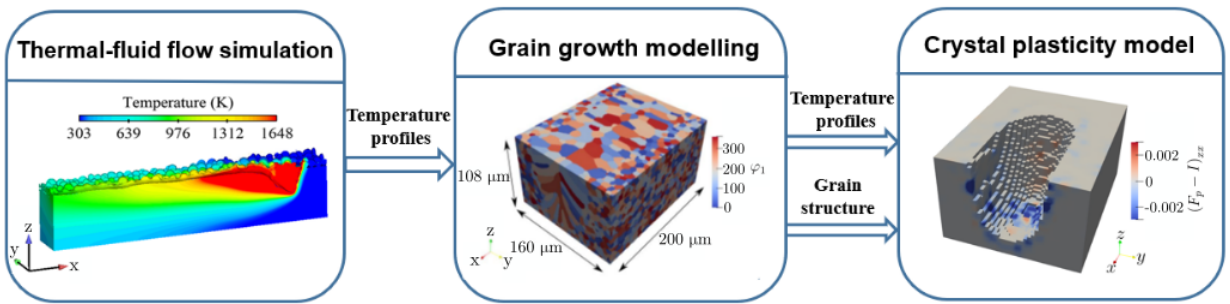


Figure 3: Flowchart of the multiscale modeling framework of the L-PBF process to determine the grain structure and deformation inside individual grains.

## 2.6. Grain selection and extraction

To investigate the dislocations dynamics at different positions in the AM part, different representative grains are selected from the phenomenological CPFEM simulation in Fig. 3. The selected crystalline grains have different deformation histories and temperature histories because of their different positions in the representative volume. The dislocation structure evolution in each grain is observed in the simulations based on the unique thermal and loading history of the grain, while the dislocation motion between grains is not considered. Therefore, by comparing them, the relationship between the formation of dislocation structures, the position in the sample and the AM process can be investigated. This is important because the formation of dislocation structures may not take place everywhere in the sample.

The selected grains are representative grains at various positions with respect to the molten pool, as shown in Fig. 4: Grain 1 is at the bottom; Grain 2 is a columnar grain near the top of the molten pool, with a horizontal top surface and an irregular shape; Grain 3 is a columnar grain that grows vertically from the bottom of the molten pool; Grain 4 is a small grain close to the lateral boundary of the domain and about 50 μm from the molten pool. The deformation and temperature history of these grains are used for the CDD simulations described in the following sections. After grain selection, the dislocation

dynamics models describing the most active slip system in each of the selected grains are set up. For each grain, the most active slip system is determined from the phenomenological CPFEM simulation, in which each selected grain is reconstructed by smoothing the lateral boundaries and by interpolating the state variables. The plastic slip rate on each slip system is averaged and used as a criterion to determine the most active slip system.

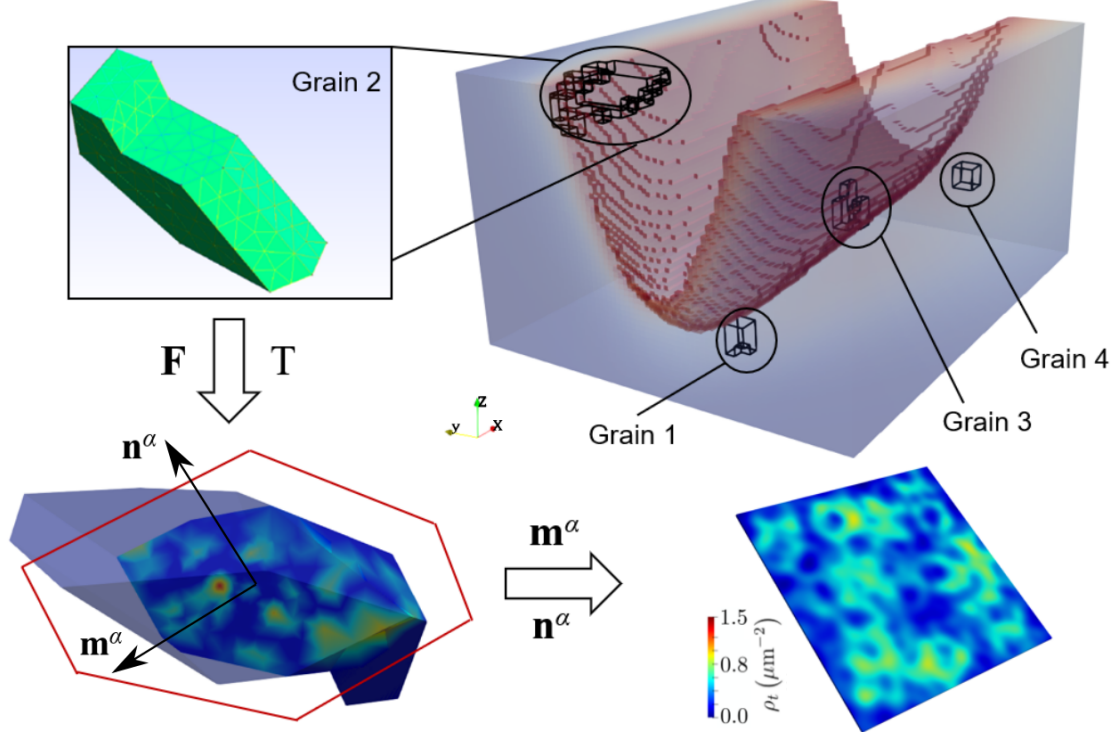


Figure 4: Schematic diagram of the strategy to build a single crystal dislocation model from the phenomenological polycrystal CPFEM simulation. Deformation gradient  $\mathbf{F}$  and temperature  $T$  are extracted from the large scale phenomenological CPFEM simulation and passed to the small scale CDD simulation.

Suppose  $\mathbf{m}^\alpha$  and  $\mathbf{n}^\alpha$  are the slip direction and normal of the most active slip system in each grain respectively. The displacement vector  $\mathbf{u}$  during the CPFEM simulation is extracted for each lateral surface of the reconstructed grain and averaged over the corresponding lateral surface. A linear interpolation of  $\mathbf{u}$  inside the volume of the grain is carried out. Each selected grain has a specific rotation matrix  $\mathbf{R}$ , which is calculated based on the Euler angles  $(\varphi_1, \Phi, \varphi_2)$  used in the phenomenological CPFEM model, which follows the  $Z_1$ - $X_2$ - $Z_3$  convention [91, 92].  $\mathbf{R}$  is used to calculate the directions of  $\mathbf{m}^\alpha$  and  $\mathbf{n}^\alpha$  in the phenomenological CPFEM simulation reference frame. Then, the displacement gradient is projected on the slip system by using  $\mathbf{m}^\alpha \cdot \nabla \mathbf{u} \cdot \mathbf{n}^\alpha$ . This provides the projected, or resolved, shear strain on the most active slip system. The average temperature inside the selected grains is also extracted because the CDD model is temperature dependent. This multiscale simulation process is schematically illustrated in Fig. 4.

To compare the effect of different deformation and temperature histories on the dis-

location dynamics, single crystal simulations are carried out for different grains using the projected shear strain extracted from the phenomenological CPFEM simulation. Two types of domains are used. The first is thinner along the slip normal direction and represents a single large slip plane: it is  $40 \mu\text{m} \times 40 \mu\text{m} \times 0.4 \mu\text{m}$  along the  $x$ ,  $y$  and  $z$  axes, with hexahedral elements of  $0.4 \mu\text{m}$ . In these simulations, the  $x$  direction corresponds to the slip direction, while the  $z$  direction is the slip plane normal of the most active slip system, which is the same convention used in the CDD model equations in Section 2.2. Therefore, the domain represents the most active slip plane in each grain. The second domain represents an entire grain, approximated as a parallelepiped. The size of this grain is extracted from the phenomenological CPFEM simulation and it is  $8 \mu\text{m} \times 8 \mu\text{m} \times 12 \mu\text{m}$  along the  $x$ ,  $y$  and  $z$  axes, with hexahedral elements of  $0.4 \mu\text{m}$ . This second domain is more computationally expensive and it is applied only to Grain 1 simulation.

The projected shear is applied as pure shear boundary conditions, i.e. the back surface ( $z = 0$ ) has  $u_x = u_y = u_z = 0$ , while the front surface has  $u_y = u_z = 0$  and displacement is applied along the  $x$  direction to reproduce the shear strain as a function of time. The initial dislocation density is created by superposing 200 dislocation loops using the method in Appendix C, each one described by equations (C.1)-(C.3) and centered in a random position on the slip plane. The parameters for the initial dislocation configuration used in this work are listed in Table 2 and the dislocation density is assumed uniform along  $z$ .

Table 2: Initial dislocation density for the single crystal simulation.

Radius of dislocation loops ( $r$ )	$3 \mu\text{m}$
Number of dislocation loops	200
Width of dislocation loops ( $w$ )	$1 \mu\text{m}$
Max loop dislocation density ( $\rho_{max}$ )	$0.2 \mu\text{m}^{-2}$

### 3. Results

#### 3.1. Dislocation dynamics in different grains

The projected shear strain on the most active slip systems of the four selected grains is shown in Fig. 5(a), and the temperature histories are included to account for the thermal effects on dislocation evolution as shown in Fig. 5(b). The difference between the total time spans of the deformation and temperature histories of different grains is due to the melting and solidification. The history of each grain is extracted after its solidification only. Since the grains at the bottom and lateral side of the molten pool do not undergo the melting-solidification process during this simulation, their histories have longer durations, as shown for Grains 1 and 4 in Fig. 5. These grains have experienced a transition from compression to tension and from heating to cooling. By contrast, Grains 2 and 3 undergo monotonic load during cooling after solidification.

Taking Grain 1 as an example, the time evolution of the dislocation density during laser scanning and cooling stage is shown in Fig. 6 for the thinner slip plane simulation. The

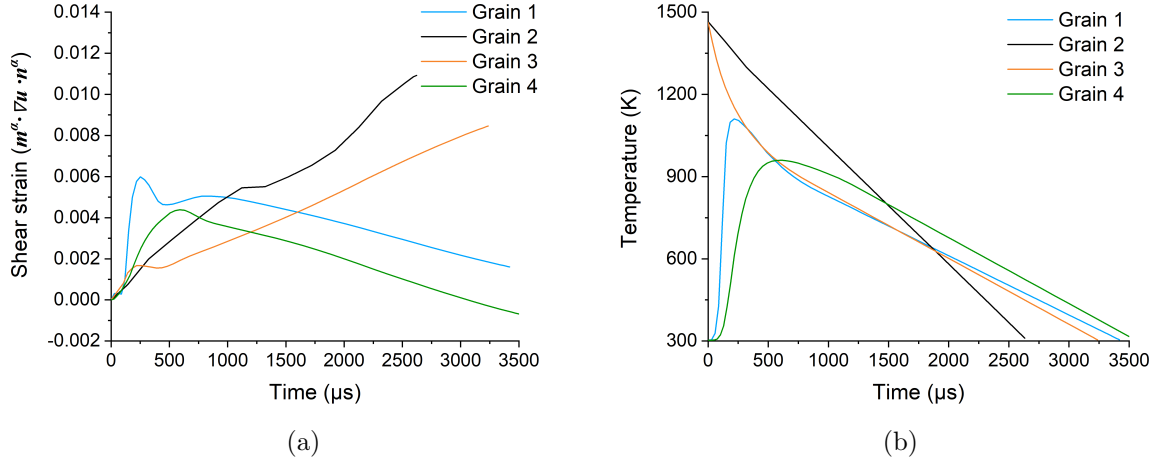


Figure 5: (a) Projected, or resolved, shear strain history of the most active slip system in each selected grain, used as a boundary condition in the CDD model simulations. (b) Temperature history of selected grains used in the temperature dependent CDD model simulations.

corresponding dislocation velocities at three representative time points are shown in Fig. 7. When Grain 1 is ahead of laser scanning, shear strain rapidly increases and the dislocation velocity is positive and up to  $0.04 \mu\text{m}/\mu\text{s}$  almost everywhere in the representative volume, apart from few spots in which the dislocation density is high. Dislocation density increases and redistributes, at  $t = 80 \mu\text{s}$  and  $t = 160 \mu\text{s}$ , and  $\rho_t$  goes up to  $1.5 \mu\text{m}^{-2}$  in some regions. When the laser passes Grain 1, after  $t \approx 600 \mu\text{s}$ , the shear strain fluctuates and then decreases steadily. As a consequence, the dislocation velocity decreases below  $0.006 \mu\text{m}/\mu\text{s}$  at  $t = 670 \mu\text{s}$ , as shown in Fig. 7. At this time point, the dislocation density is stable and dislocation pattern is clear in Fig. 6(b), which is constituted by cellular regions with the dislocation density up to  $4.5 \mu\text{m}^{-2}$ . Some of these cellular regions are connected to each other, while others are surrounded by low density regions with the density as low as  $2.5 \mu\text{m}^{-2}$ . The dislocation density remains stable until  $t = 1170 \mu\text{s}$ , and then starts evolving because of the additional thermal stress during the cooling stage. In this stage, the shear strain decreases, as shown in Fig. 5(a). Therefore, the dislocation velocity becomes negative, as shown in Fig. 7 at  $t = 1550 \mu\text{s}$ , while the dislocation curvature is still positive. This leads to a decrease of the dislocation density because of the source term on the right-hand side of equation (10), as shown in Fig. 6(c) at  $t = 1990 \mu\text{s}$ . From  $t = 1990 \mu\text{s}$  to the end  $t = 3420 \mu\text{s}$ , further rearrangement of the dislocation structures takes place and the final result is shown in the pattern of Grain 1 in Fig. 9. There are about 10 high-dislocation-density cellular regions and the same number of low density regions. Therefore, we can deduce that the characteristic periodicity of the high and low dislocation density regions is about  $12.6 \mu\text{m}$ . That is, cellular regions, i.e., the red regions in the pattern of Grain 1 in Fig. 9, have an average diameter of  $6.3 \mu\text{m}$ . These simulations show that the mechanisms introduced in the evolution equations (10)-(13) and the CRSS equation (5) are sufficient to reveal the

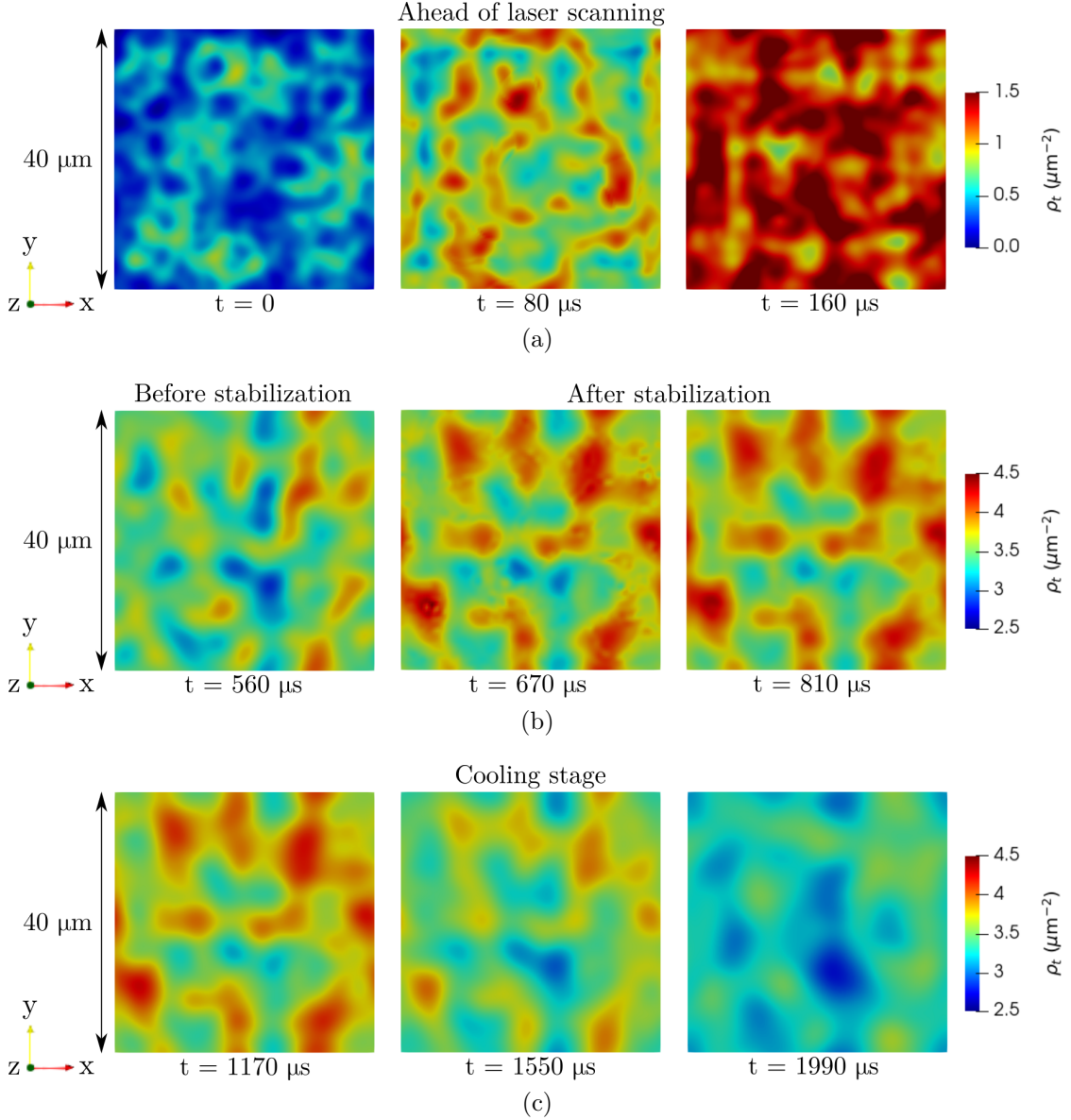


Figure 6: Evolution of the total dislocation density  $\rho_t$ : (a) when the grain is ahead of the laser beam and the temperature is increasing, (b) after the temperature peak, when the first stabilization of the dislocation structures occurs, (c) during the cooling stage, when the motion of the dislocations restarts after the stabilization phase.

formation of dislocation structures during AM process.

The evolution of the average dislocation density for the selected grains is shown in Fig. 8. It can be seen that the growth rate of the dislocation density conforms to the trend of the shear strain, and the dislocation density on the slip plane increases with the increase of the shear strain, which is correlated with the temperature field. Through the comparison of different grains, it can be found that the grain on the top surface, Grain 2, has the

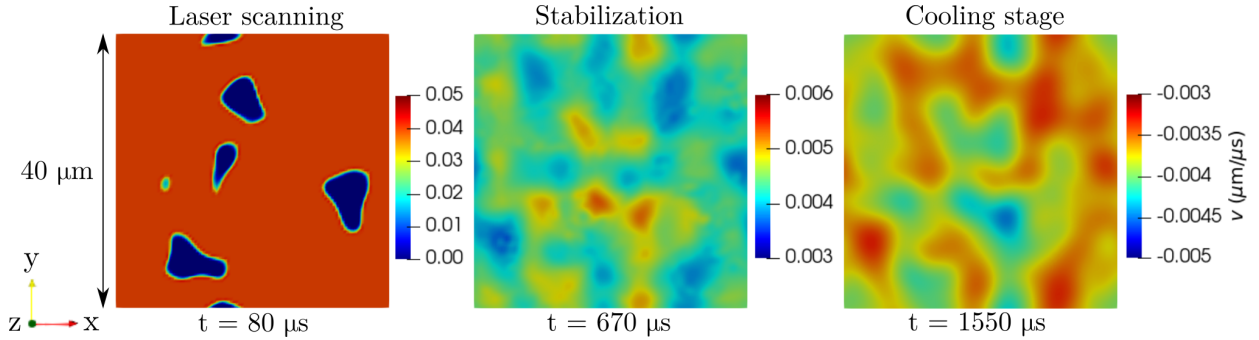


Figure 7: Dislocation velocity at three different time points: during laser scanning, just before the first stabilization occurs and during the cooling stage.

largest strain after solidification. Several factors contribute, such as the proximity to the unconstrained upper surface and to the molten pool. Grain 2 shows the largest increase of the dislocation density, which is correlated with the largest increase of the shear strain. Grains that are further away from the molten pool and do not melt, e.g., Grain 1 below the bottom of the molten pool and Grain 4 on the side, experience fluctuations in the dislocation density during the heating-cooling cycle. In Grain 1 and 4, the average dislocation density increases sharply during heating, but then decreases during the cooling stage. Grain 2 and 3 are in the molten pool, so only the loads after solidification are considered. Grain 2 and 3 are subject to large and monotonic shear strains during the cooling stage, which cause large residual stresses [57]. Therefore, these grains exhibit larger dislocation density growth during the laser scanning process, corresponding to greater plastic deformations.

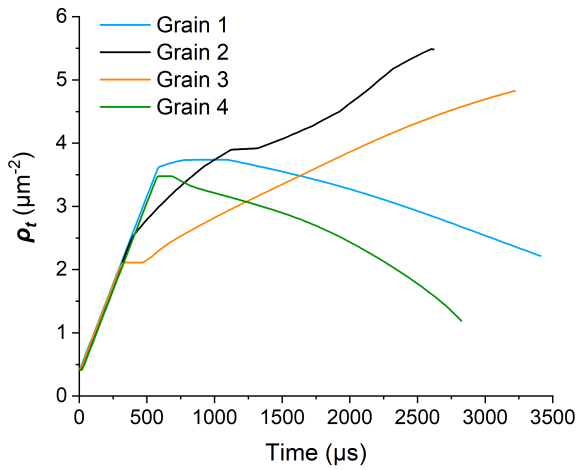


Figure 8: Average dislocation density evolutions on the slip plane of selected grains.

The final dislocation patterns of the selected grains are shown in Fig. 9. It can be found that the grains at different positions have different final dislocation patterns after cooling. Grain 1 and Grain 4, which are outside of the molten pool and do not undergo melting,

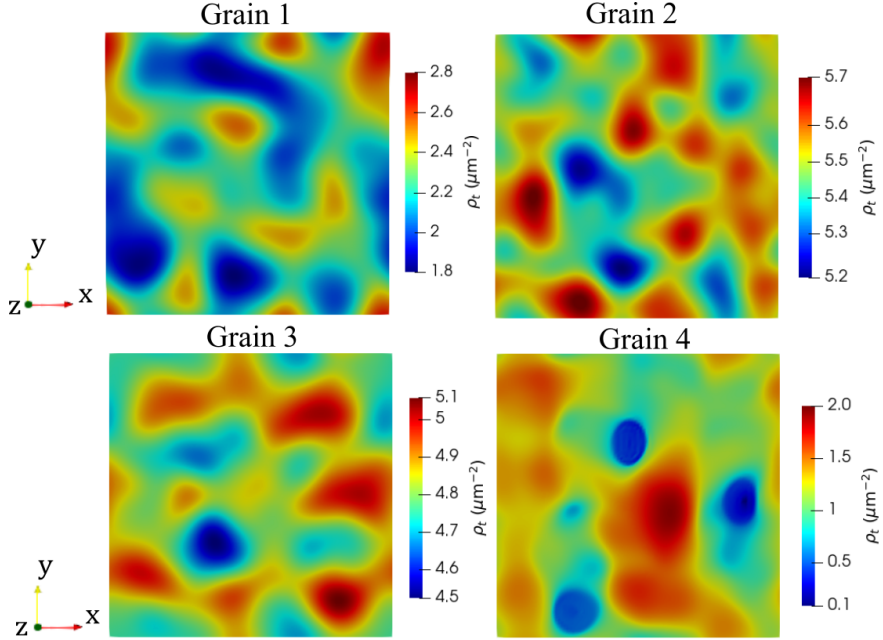


Figure 9: Different final dislocation structures in the selected grains after laser scan and cooling stage.

have lower dislocation densities than the other grains; this is because their loading histories are not monotonic. The dislocation densities of the Grain 2 and 3 are somewhat similar because of the monotonic load history after solidification. The difference between them is that the magnitudes of deformation and temperature change are different due to their different depths in the molten pool. As shown in Fig. 5(a), Grain 2 has experienced more deformation on the top surface and thus has a higher final dislocation density than others.

The presence of dislocation structures is indicated by the ratio between the dislocation densities  $\rho_t$  in high and low density regions. As shown in Fig. 9, the dislocation structures are less evident in Grain 2 and 3, while Grain 1 and Grain 4 exhibit more clear dislocation patterns. In particular, Grain 4 shows low-dislocation-density cells with  $\rho_t$  as low as  $0.1 \mu\text{m}^{-2}$ . Therefore, these simulations indicate that grains that do not undergo melting during the laser scanning process are expected to contain well defined dislocation cellular structures. This is associated with the cyclic loads they undergo. However, grains that have solidified during the laser scan, like Grain 2 and 3, are expected to contain a larger number of dislocations.

The full grain simulation results of Grain 1 are shown in Fig. 10. The model is reproduced according to its dimensions in the polycrystal CPFEM simulation. Given the similar initial dislocation density as well as the deformation and temperature history obtained at grain scale, it can be seen from Fig. 10 that the full grain simulation provides similar dislocation stabilization as shown by the thinner slip plane results in Fig. 6. The results of the full grain simulation show that during AM process, the dislocation structures inside the grain can rearrange and stabilize; afterwards they gradually decrease in size during cooling. The formation and stabilization of the unique cell observed in the full grain simulation takes

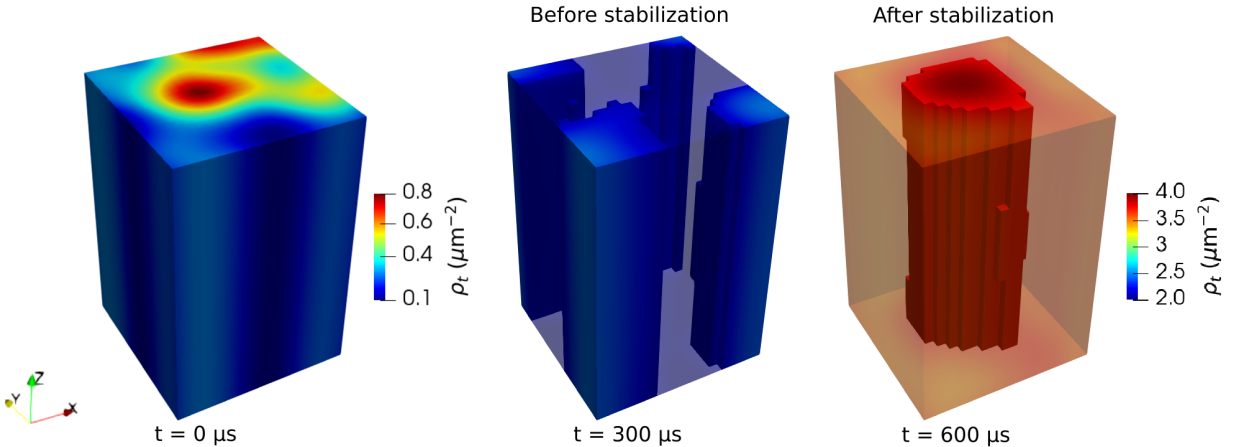


Figure 10: Total dislocation density  $\rho_t$  in the full grain simulation at  $t = 0 \mu\text{s}$ ,  $t = 300 \mu\text{s}$ , before stabilization, and  $t = 600 \mu\text{s}$ , after stabilization of the dislocation structures.

place between  $t = 300 \mu\text{s}$  and  $t = 600 \mu\text{s}$ , which is slightly earlier than the stabilization of the multiple cells in the thinner slip plane simulation. The assembly and stabilization of the high-density dislocation cells conform to the observation in the experimental works [93, 19]. However, the full grain simulations require much higher computational cost. Since in this work we are not aiming at investigating the dislocation distribution in the slip plane normal direction, thinner slip plane models are applied for subsequent simulations.

### 3.2. Effect of dislocation annihilation

The dislocation annihilation mechanism is not included in the reference simulations of Grain 1 in Section 3.1 and is introduced individually in this section to understand the effect on the dislocation dynamics and dislocation structures formation.

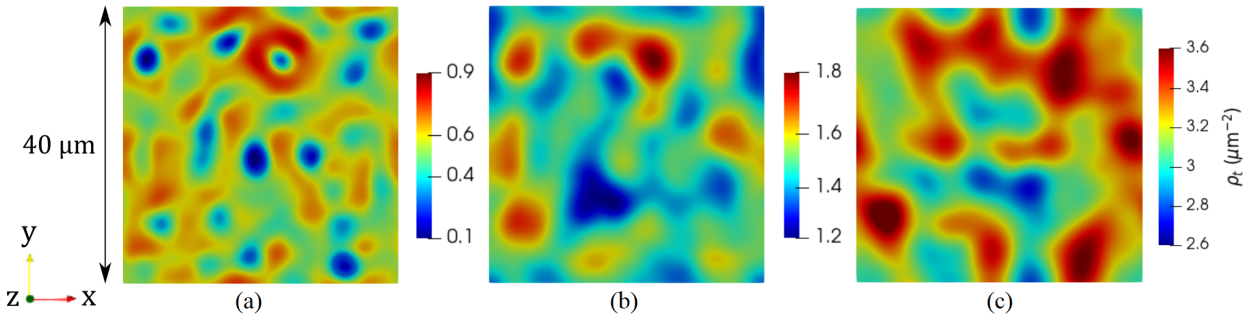


Figure 11: Dislocation structures with different annihilation distances (a)  $\check{d}_c = 25 \text{ nm}$ , (b)  $\check{d}_c = 12.8 \text{ nm}$ , (c)  $\check{d}_c = 1.3 \text{ nm}$  at time  $t = 1550 \mu\text{s}$ .

Since the annihilation mechanisms of edge and screw dislocations are different [80, 81], the annihilation distances of edge and screw dislocations in 316L SS are reported to be 1.3 nm and 50 nm respectively [82, 83, 94]. In the current model, a unique term is used for the annihilation of the total dislocation density  $\rho_t$ , as shown in equation (23), while edge and

screw dislocations are not distinguished in the annihilation term. Thus, some intermediate values of the annihilation distance  $\tilde{d}_c$  including 25 nm, 12.8 nm and 1.3 nm are selected and tested with the Grain 1 simulation. Comparing the results with annihilation in Fig. 11 with the one without annihilation shown in Fig. 6(c), at the same time point ( $t = 1550 \mu\text{s}$ ), the annihilation mechanism can lead to a significant reduction of the dislocation density. As shown in Fig. 11(a)-(c), with the decrease of the annihilation distance, the overall dislocation density increases, revealing that the annihilation effect is weakened. Meanwhile, the low-dislocation-density regions become more connected, and thus the characteristic length scale of the dislocation structures increases. The ratio between regions with high and low dislocation densities is largest for  $\tilde{d}_c = 25 \text{ nm}$ ; in this case, small cellular regions with dislocation density close to zero form, as shown in Fig. 11(a).

### 3.3. Effect of mechanical loading

As reported in [14, 15], the unique dislocation network in AM parts leads to the improvement of both the strength and ductility, because the pre-existing dislocation network can maintain its configuration, impede but not entirely block the dislocation motion in the cellular structure. To investigate whether the dislocation structures after the AM process are stable, a mechanical loading simulation is carried out after the cooling stage of the Grain 1 simulation in Fig. 9. A unidirectional shear strain, with component  $\varepsilon_{xz}$ , is applied to the simulation domain.

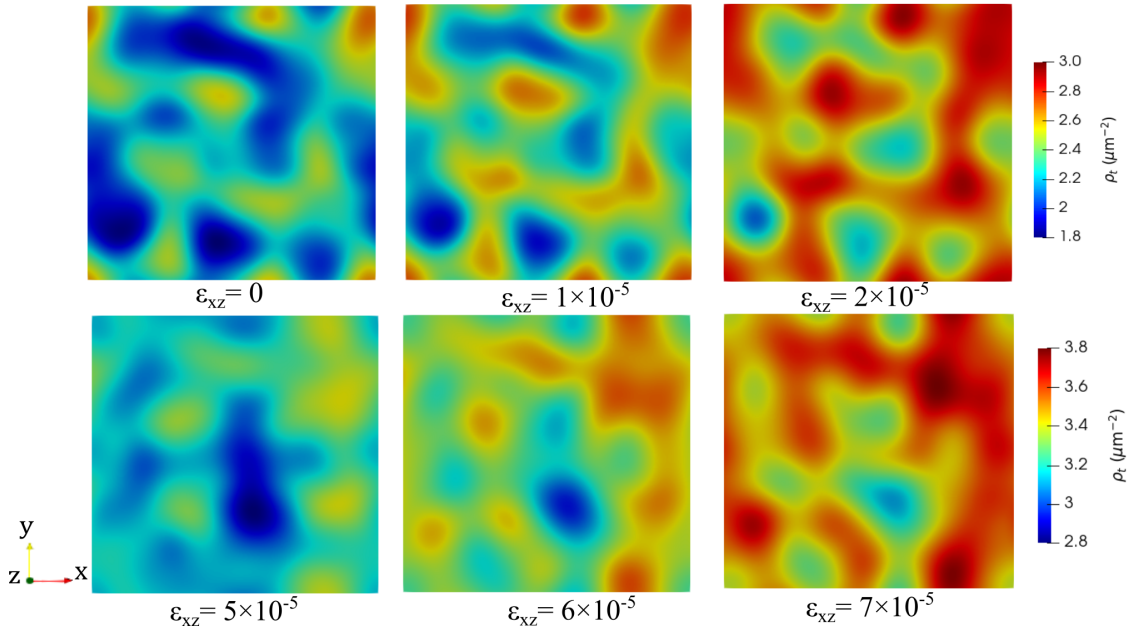


Figure 12: Dislocation evolution on the slip plane during the mechanical loading process.

As shown in Fig. 12, during the loading process, starting from the dislocation pattern of the reference simulation at  $t = 3420 \mu\text{s}$ , the dislocations keep evolving and the dislocation density increases. The high density region becomes more connected but the shape of the

dislocation structures is roughly maintained up to  $\varepsilon_{xz} = 2 \times 10^{-5}$ . Due to the continuous movement of dislocations, the dislocation structures gradually change shape as time evolves, and finally forms a dislocation distribution with a higher overall dislocation density. As shown in Fig. 12, the dislocation structures at  $\varepsilon_{xz} = 7 \times 10^{-5}$  have gradually evolved from the initial dislocation structures; the dislocation patterns at the two different moments are different. These simulations predict that the dislocation structures are stable until a certain threshold load is reached, and afterwards they gradually evolve to accommodate larger plastic deformations.

### 3.4. Effect of cyclic thermal loading in multi-layer AM process

During fabrication of AM parts, most grains are subjected to multiple heating-cooling cycles, which in turn promote further development of dislocations eventually forming unique dislocation networks in the material. In this work, in order to study the influence of multi-layer AM process, a cyclic loading simulation is carried out by selecting grains at different depths in the L-PBF 316L SS case. It should be pointed out that in the realistic AM process, the thermal fields caused by multi-layer and multi-track fabrication affect the grain deformation and dislocation dynamics together. This section focuses on the cyclic loading caused by the multi-layer thermal field at different depths, thus the multi-track or layer-rotation cases are not involved.

Grain 2 in Fig. 4 is firstly selected as an example of grain in the top layer of the multi-layer fabrication, and then three more grains beneath Grain 2 are selected every 30  $\mu\text{m}$ , which is the layer thickness of the L-PBF 316L stainless steel experiment in this work [7]. The deformation and temperature histories of those four grains at different depths are extracted from the phenomenological CPFEM simulation. These histories are concatenated, starting from Grain 2 to the grain at the bottom, while maintaining continuity as shown in Fig. 13(a)-(b). Since four grains are selected in total, this approach represents a 4-layer cyclic simulation. The 4-layer thermal stress loading and temperature histories are used as the continuous deformation and temperature that a single grain experiences during multi-layer fabrication as shown in Fig. 13(a) and (b). The cyclic simulation is carried out with the same initial dislocation distribution reported in Section 3.1, constituted of 200 positively curved dislocation loops. The simulation has been carried out with and without the dislocation annihilation mechanisms, using an annihilation distance  $\check{d}_c = 1.3 \text{ nm}$ .

As shown in Fig. 13(c), the evolution of the average dislocation density on the slip plane without annihilation is consistent with the variation trend of shear strain and temperature, thus the dislocation density peak at the last cycle becomes lower than the previous ones. With increasing cycle number, the average dislocation density slightly decreases due to negative dislocation velocity in cooling stage. When dislocation annihilation with  $\check{d}_c = 1.3 \text{ nm}$  is included, the evolution of average dislocation density is shown in Fig. 13(d), which is more realistic for the dislocation evolution in multi-layer AM process. The highest average dislocation density occurs when the grain solidifies and cools down before the further reheating-cooling cycles of this grain.

In Fig. 14, the dislocation patterns at the end of each cycle with annihilation are presented. At the beginning of each cycle, the dislocation structures formed in the cooling

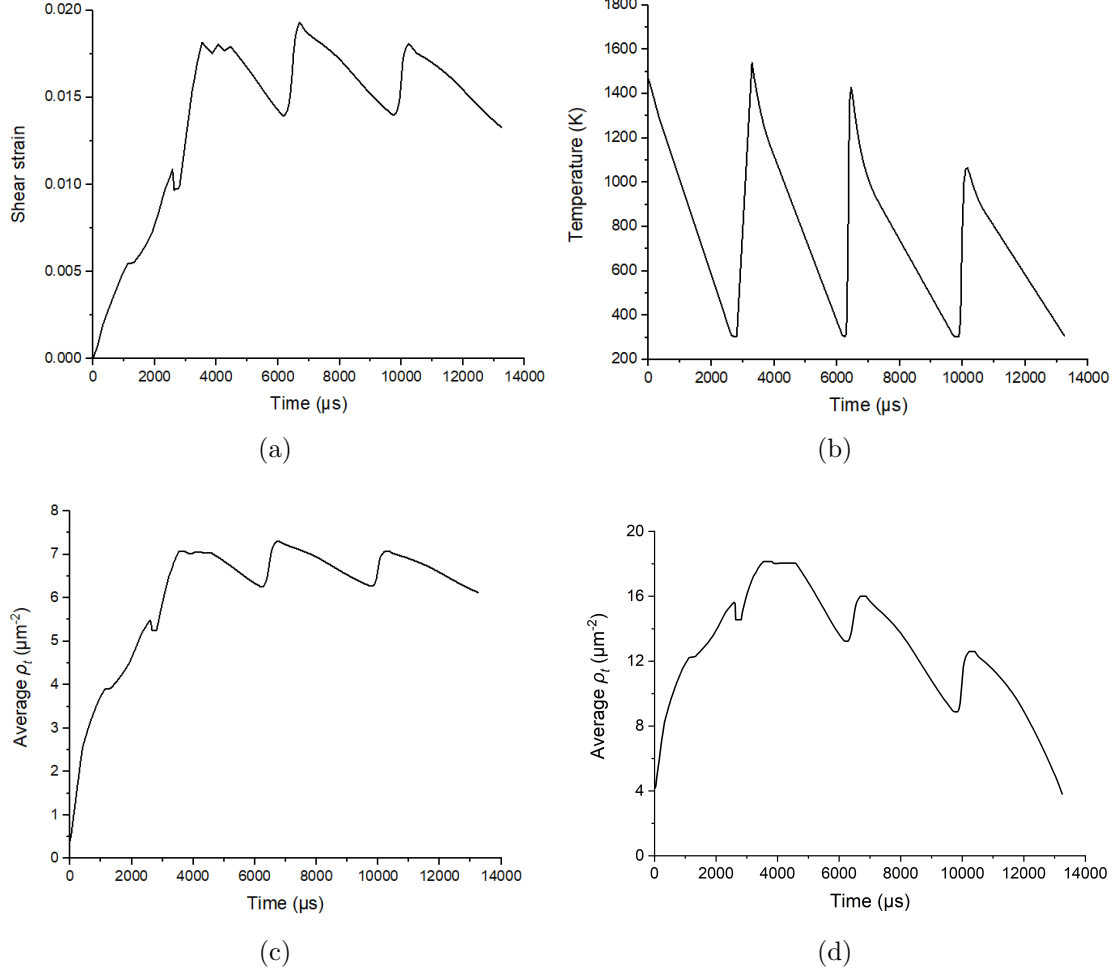


Figure 13: Cyclic thermal loading simulation to resemble multi-layer AM process: (a) Projected shear strain and (b) temperature history for multi-layer AM process as the input of the simulation. Simulation results: (c) average dislocation density on the slip plane. (d) average dislocation density on the slip plane with annihilation mechanism.

stage of the previous cycle rapidly redistribute due to the heating and the increasing shear strain, which cause a significant dislocation motion. It can be found that the characteristic length of the dislocation structures increases after the first cycle, as compared with the initial distribution in Fig. 6. After more cycles, the cellular structures become larger with an increasing ratio between high and low dislocation density regions. On the one hand, this reveals the formation of dislocation structures in the multi-layer fabrication process that gradually evolve into the final patterns over multiple heating-cooling cycles. On the other hand, this result also reveals the effect of the annihilation mechanism. This mechanism is necessary to obtain low dislocation density regions surrounding the cellular structures. More cyclic thermal loading simulations have been carried out using higher values of  $\check{d}_c$  and it has been observed that the ratio between  $\rho_t$  in high and low dislocation density regions increases

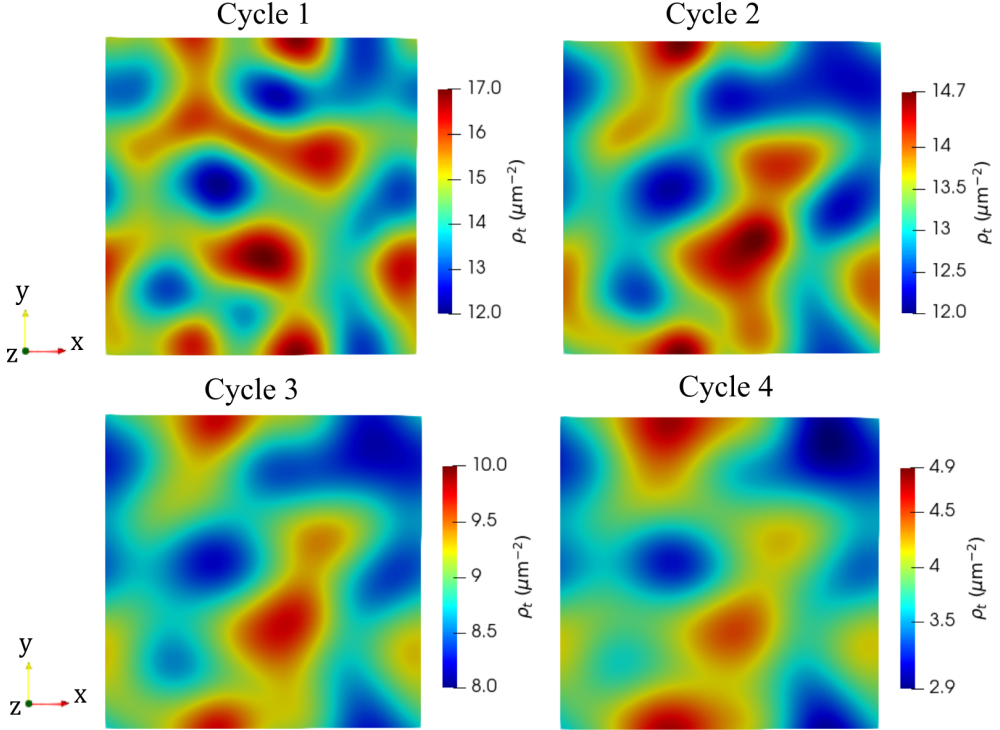


Figure 14: Dislocation patterns at the end of each cycle in the multi-layer cyclic thermal loading simulation.

significantly. Applying more thermal cycles would also lead to low density regions with  $\rho_t$  closer to zero.

#### 4. Discussion

Previous works have pointed out that the thermal expansion and shrinkage are the primary sources of dislocations in AM parts [19], and the plastic deformation induced by large residual stress would lead to high-density dislocation accumulation [18]. This work supports those conclusions by simulating a microscale domain representing a single slip system inside a single grain during the AM process. The present model does not include the effect of micro-segregation and precipitation, but the dislocation structures can still form in AM process. The mechanisms modeled by equations (10)-(13), such as dislocation multiplication and interactions, are therefore sufficient for the dislocation structures formation in AM process.

Following the formation, stable dislocation structures are observed during cooling as reported in Section 3.1. These grains undergo non-unidirectional cyclic deformations during the multi-layer fabrication. Therefore, most of the grains in the bulk may form stable dislocation structures, which stabilize during multiple re-heating-cooling cycles. This can be one reason why dislocation structures in the AM parts appear more stable than those in the parts manufactured by traditional techniques [15]. In the subsequent mechanical loading during service, which may have a smaller magnitude than the thermally induced

deformation during the AM process and a lower strain rate, the stable dislocation structures are not easily destroyed before the plastic deformation exceeds a threshold value, as revealed by the simulations in Section 3.3.

The growth of the dislocation density of the grains in the molten pool mainly comes from the thermal stress after solidification. Since the thermal stress inside the molten pool is usually higher [57], the dislocation density of the grains in this region increases more than those of other grains during the cooling stage. The largest increase in dislocation density occurs when the grain is on the unconstrained top surface of the sample, but the dislocation density during multi-layer fabrication roughly depends on the dislocation density increase during the first thermal cycle after solidification, according to Section 3.4. During subsequent reheating and cooling cycles, the dislocation density does not increase significantly, and can even decrease due to annihilation, as shown in Fig. 13(d).

The dislocation annihilation has an important effect on both the dislocation density evolution and the characteristic size of the dislocation structures. Since the current model cannot distinguish the different annihilation distances of edge and screw dislocations, a parametric analysis using intermediate values is carried out in Section 3.2. A larger dislocation annihilation distance increases the ratio between high and low dislocation density regions and leads to more connected cellular structures. Dislocation annihilation appears to be a necessary mechanism for the formation of cellular regions with a dislocation density close to zero, as observed in experiments [15].

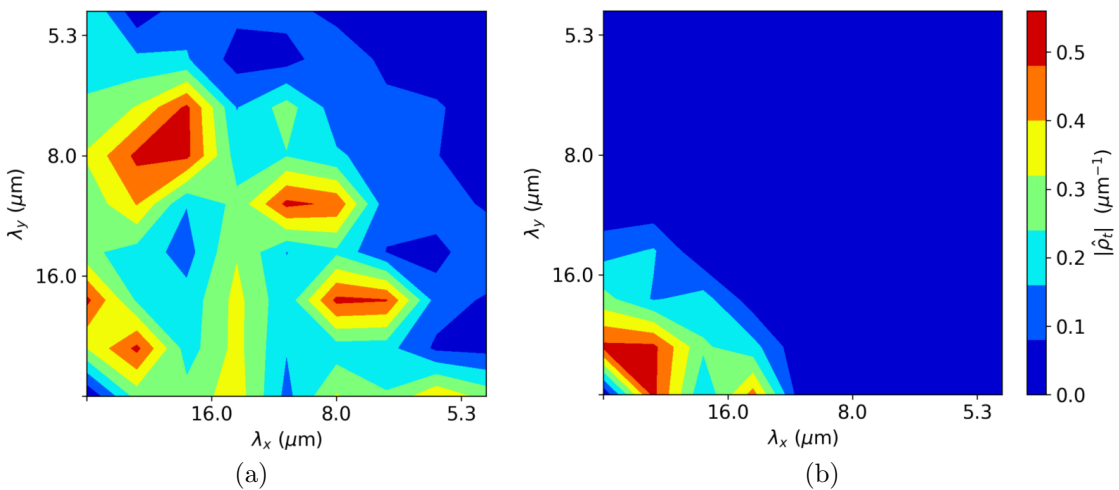


Figure 15: Length scale analysis by Fourier analysis of the simulation results: (a) with annihilation distance  $\check{d}_c = 25$  nm, shown in Fig. 11(a); (b) multi-layer simulation after 4 cycles, shown in Fig. 14.

To analyze the characteristic length scale of the dislocation structures, the Fast Fourier Transform (FFT) of the simulated total dislocation density  $\rho_t$  is calculated in the  $x$ - $y$  plane, as shown in Fig. 15. As shown in the following, the same analysis is carried out on several experimental images available in the literature. In that case, the FFT is calculated by assuming that the total dislocation density is directly proportional to the intensity of

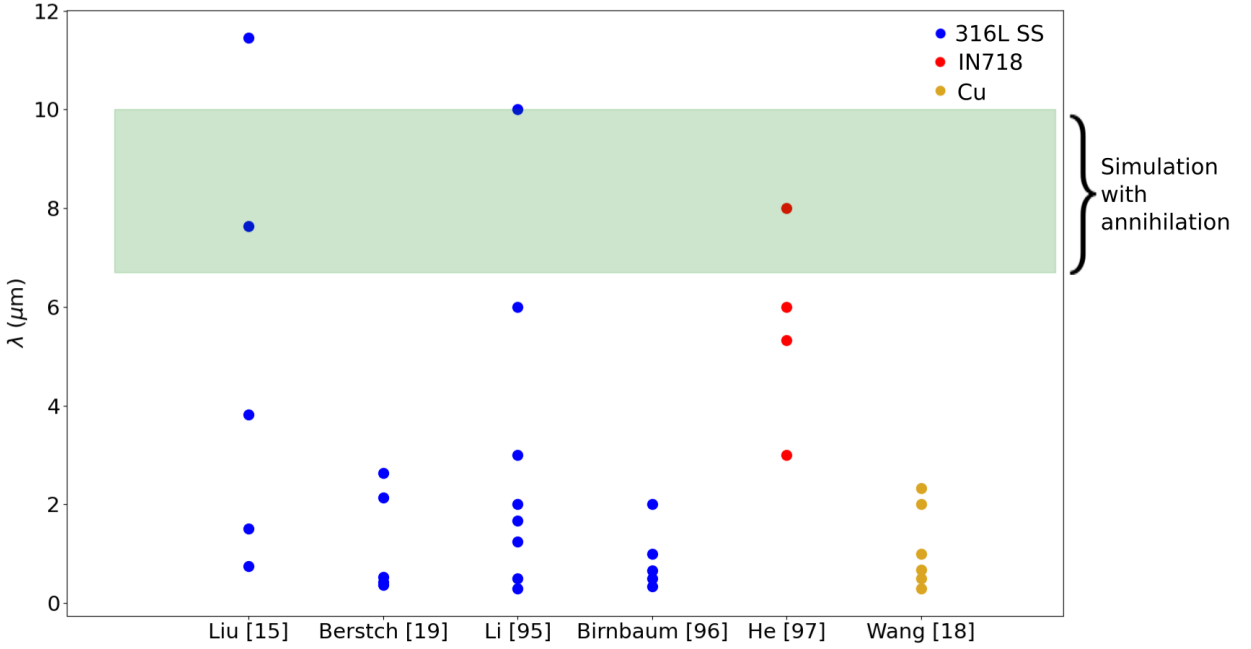


Figure 16: Comparison of the characteristic length scales of the dislocation structures observed in previous experiments of different additively manufactured materials (316L SS [15, 19, 95, 96], Inconel 718 [97] and copper [18]) and simulations in this work.

the black color at each point in the image plane. Several experimental results are used, as shown in Fig. 16. The characteristic length scales of the simulated results are extracted from Fig. 11(a), which represents the slip plane simulation with  $\bar{d}_c = 25 \text{ nm}$ , and Fig. 14 (cycle 4 of the cyclic simulation) respectively. The FFT of the slip plane simulation with annihilation shows several peaks: some of them are in the range between  $6.7 \mu\text{m}$  and  $10 \mu\text{m}$ , which is in the same order of magnitude of the characteristic size of dislocation structures as collected in previous experimental works of AM 316L SS [15, 19, 95]. By contrast, a peak around the length scale of  $12 \mu\text{m}$  is present in the multi-layer simulation. This shows that the cyclic thermal load increases the characteristic size of dislocation structures by a factor two or more. By performing FFT analysis on the dislocation structure size of different additively manufactured materials as shown in Fig. 16, it can be found that although most of the dislocation structure sizes in the AM materials are no more than  $6 \mu\text{m}$ , the simulated characteristic size range still agrees with some of the larger experimental dislocation structure sizes ranging from  $6$  to  $12 \mu\text{m}$ , which shows that this model is reasonable for dislocation structure reproduction in AM parts. Even for different materials such as IN718 and copper fabricated by AM, the length scale of the observed dislocation structures is in this universal range with some sample-to-sample variations. It is expected that, for AM materials, the dislocation structure size can be tuned by the different process parameters, however the present simulations analyze only one set of process parameters and future studies may extend the present approach to different manufacturing conditions. The comparison also suggests that the small length scale of the experimental dislocation structures can be caused by the pres-

ence of significant dislocation annihilation, thus it is necessary to consider the annihilation mechanism to get dislocation structures with realistic sizes when simulating the dislocation dynamics of AM parts. As stated in Section 3.2, a larger annihilation length would lead to smaller dislocation structures, therefore it would be beneficial to find an annihilation length for the simulations to match the experimental results for the different materials. Since in this work the different types of annihilation are expressed by an intermediate value, this model could be further improved by distinguishing annihilation lengths of edge and screw dislocations. It should also be mentioned that the element size in the simulations,  $0.4 \mu\text{m}$ , is not sufficient to resolve features smaller than this characteristic length. Therefore, this model still has the potential to be further improved for different materials, smaller scales, and more specific experimental validation.

Although this study presents a variety of simulations of the dislocation evolution inside grains during AM, there are still some limitations that need to be further addressed. Since most of the grains in AM have undergone the melting-solidification process, it is difficult to experimentally monitor the dislocation information during fabrication. Therefore, the simulations in this work can only reveal the trend and characteristics of the dislocation evolution, by assuming the initial condition after solidification. The simulation results have been roughly compared to existing experimental results, but different AM process parameters can lead to very different microstructures as well as different dislocation patterns. The effect of different input energies in the AM process, determined by laser powers and scanning speeds, on the dislocation density and dislocation structure is a worthwhile research topic for manipulating dislocation networks in AM parts. In addition, the further development of this model to improve its computational efficiency, thereby enlarging the size of the simulation domain, is desirable.

## 5. Conclusions and outlook

In this work, a computational approach to reveal the dislocation evolution of grains in AM parts is developed. This approach incorporates crystal plasticity model with a continuum dislocation dynamics model via a hybrid continuous and discontinuous Galerkin method, and is embedded into a multiscale computational framework for L-PBF simulations. The model used in this work is an extension and advancement of existing CDD models, which effectively captures the discontinuity in the evolution of dislocation variables. The effects of annihilation mechanism on the dislocation structure formation during AM process are investigated. The combination of the microscale model with the multiscale L-PBF model will have broader applications in the future.

The simulation results show the formation and evolution of the dislocation structure in the selected representative grains in AM parts. Especially, the stability of the dislocation structures in AM process within a certain temperature range and deformation amplitude is clarified as revealed by the slip plane model in Section 3.1. This provides new insights into the formation mechanisms of dislocation networks and into the performance of materials fabricated by L-PBF. Finally, this model can also be extended to investigate the evolution of dislocation structures in other metals produced using AM. This work provides a promising

guideline to tune the dislocation networks in AM materials for improving their mechanical properties.

## 6. Acknowledgement

This research is supported by the Ministry of Education, Singapore, under its Academic Research Fund Tier 2 (MOE-T2EP50120-0012).

## Appendix A. Weak form of the dislocation density evolution equations

The weak form of equation (11) can be written as:

$$\sum_E \int_{\Omega_E} \frac{\partial \rho_e}{\partial t} \Psi \, dV = - \sum_F \int_{\partial \Omega_F} \begin{pmatrix} \rho_t v \\ 0 \end{pmatrix} \cdot \hat{\mathbf{n}} \Psi \, dS + \sum_E \int_{\Omega_E} \begin{pmatrix} \rho_t v \\ 0 \end{pmatrix} \cdot \nabla \Psi \, dV . \quad (\text{A.1})$$

Because of the discontinuity of the dislocation density variables on the inner boundaries  $\partial \Omega_F$ , a flux term  $\mathbf{F}_{\partial \Omega_F}^{(\rho_e)}$  is defined by analogy with equations (15) and (20):

$$- \int_{\partial \Omega_F} \begin{pmatrix} \rho_t v \\ 0 \end{pmatrix} \cdot \hat{\mathbf{n}} \Psi \, dS = -\mathbf{F}_{\partial \Omega_F}^{(\rho_e)} \cdot \hat{\mathbf{n}} = -\mathbf{F}_{\partial \Omega_E}^{(\rho_e)} \cdot \hat{\mathbf{n}} - \mathbf{F}_{\partial \Omega_N}^{(\rho_e)} \cdot \hat{\mathbf{n}} . \quad (\text{A.2})$$

$$\mathbf{F}_{\partial \Omega_E}^{(\rho_e)} = \begin{pmatrix} v (\rho_e^+|_{\partial \Omega_E} + \rho_e^-|_{\partial \Omega_N}) \Psi_{\partial \Omega_E}^{(\rho_e)} H(v \hat{n}_x) \\ 0 \end{pmatrix} + \begin{pmatrix} v (\rho_e^+|_{\partial \Omega_N} + \rho_e^-|_{\partial \Omega_E}) \Psi_{\partial \Omega_E}^{(\rho_e)} H(-v \hat{n}_x) \\ 0 \end{pmatrix} \quad (\text{A.3})$$

$$\mathbf{F}_{\partial \Omega_N}^{(\rho_e)} = - \begin{pmatrix} v (\rho_e^+|_{\partial \Omega_E} + \rho_e^-|_{\partial \Omega_N}) \Psi_{\partial \Omega_N}^{(\rho_e)} H(v \hat{n}_x) \\ 0 \end{pmatrix} - \begin{pmatrix} v (\rho_e^+|_{\partial \Omega_N} + \rho_e^-|_{\partial \Omega_E}) \Psi_{\partial \Omega_N}^{(\rho_e)} H(-v \hat{n}_x) \\ 0 \end{pmatrix} \quad (\text{A.4})$$

The weak form of equation (12) can be written as:

$$\sum_E \int_{\Omega_E} \frac{\partial \rho_s}{\partial t} \Psi^{(\rho_s)} \, dV = - \sum_F \int_{\partial \Omega_F} \begin{pmatrix} 0 \\ \rho_t v \end{pmatrix} \cdot \hat{\mathbf{n}} \Psi^{(\rho_s)} \, dS + \sum_E \int_{\Omega_E} \begin{pmatrix} 0 \\ \rho_t v \end{pmatrix} \cdot \nabla \Psi^{(\rho_s)} \, dV , \quad (\text{A.5})$$

$$- \int_{\partial \Omega_F} \begin{pmatrix} 0 \\ \rho_t v \end{pmatrix} \cdot \hat{\mathbf{n}} \Psi^{(\rho_s)} \, dS = -\mathbf{F}_{\partial \Omega_F}^{(\rho_s)} \cdot \hat{\mathbf{n}} = -\mathbf{F}_{\partial \Omega_E}^{(\rho_s)} \cdot \hat{\mathbf{n}} - \mathbf{F}_{\partial \Omega_N}^{(\rho_s)} \cdot \hat{\mathbf{n}} . \quad (\text{A.6})$$

The flux term is defined as:

$$\mathbf{F}_{\partial \Omega_E}^{(\rho_s)} = \begin{pmatrix} 0 \\ v (\rho_s^+|_{\partial \Omega_E} + \rho_s^-|_{\partial \Omega_N}) \Psi_{\partial \Omega_E}^{(\rho_s)} H(v \hat{n}_y) \end{pmatrix} + \begin{pmatrix} 0 \\ v (\rho_s^+|_{\partial \Omega_N} + \rho_s^-|_{\partial \Omega_E}) \Psi_{\partial \Omega_E}^{(\rho_s)} H(-v \hat{n}_y) \end{pmatrix} \quad (\text{A.7})$$

$$\mathbf{F}_{\partial\Omega_N}^{(\rho_s)} = - \begin{pmatrix} 0 \\ v(\rho_s^+|_{\partial\Omega_E} + \rho_s^-|_{\partial\Omega_N}) \Psi_{\partial\Omega_N}^{(\rho_s)} H(v\hat{n}_y) \end{pmatrix} - \begin{pmatrix} 0 \\ v(\rho_s^+|_{\partial\Omega_N} + \rho_s^-|_{\partial\Omega_E}) \Psi_{\partial\Omega_N}^{(\rho_s)} H(-v\hat{n}_y) \end{pmatrix} \quad (\text{A.8})$$

The weak form of the first two terms on the right-hand side of equation (13) is:

$$-\sum_F \int_{\partial\Omega_F} \begin{pmatrix} v\rho_e q_t/\rho_t \\ v\rho_s q_t/\rho_t \end{pmatrix} \cdot \hat{\mathbf{n}} \Psi^{(q_t)} dS + \sum_E \int_{\Omega_E} \begin{pmatrix} v\rho_e q_t/\rho_t \\ v\rho_s q_t/\rho_t \end{pmatrix} \cdot \nabla \Psi^{(q_t)} dV. \quad (\text{A.9})$$

The flux term is defined as:

$$-\int_{\partial\Omega_F} \begin{pmatrix} v\rho_e q_t/\rho_t \\ v\rho_s q_t/\rho_t \end{pmatrix} \cdot \hat{\mathbf{n}} \Psi^{(q_t)} dS = -\mathbf{F}_{\partial\Omega_F}^{(q_t,1)} \cdot \hat{\mathbf{n}} = -\mathbf{F}_{\partial\Omega_E}^{(q_t,1)} \cdot \hat{\mathbf{n}} - \mathbf{F}_{\partial\Omega_N}^{(q_t,1)} \cdot \hat{\mathbf{n}}. \quad (\text{A.10})$$

$$\mathbf{F}_{\partial\Omega_E}^{(q_t,1)} = \begin{pmatrix} vq_t(\rho_e^+|_{\partial\Omega_E} - \rho_e^-|_{\partial\Omega_N}) \Psi_{\partial\Omega_E}^{(q_t)} H(v\hat{n}_x)/\rho_t \\ vq_t(\rho_s^+|_{\partial\Omega_E} - \rho_s^-|_{\partial\Omega_N}) \Psi_{\partial\Omega_E}^{(q_t)} H(v\hat{n}_y)/\rho_t \end{pmatrix} + \begin{pmatrix} vq_t(\rho_e^+|_{\partial\Omega_N} - \rho_e^-|_{\partial\Omega_E}) \Psi_{\partial\Omega_E}^{(q_t)} H(-v\hat{n}_x)/\rho_t \\ vq_t(\rho_s^+|_{\partial\Omega_N} - \rho_s^-|_{\partial\Omega_E}) \Psi_{\partial\Omega_E}^{(q_t)} H(-v\hat{n}_y)/\rho_t \end{pmatrix} \quad (\text{A.11})$$

$$\mathbf{F}_{\partial\Omega_N}^{(q_t,1)} = -\begin{pmatrix} vq_t(\rho_e^+|_{\partial\Omega_E} - \rho_e^-|_{\partial\Omega_N}) \Psi_{\partial\Omega_N}^{(q_t)} H(v\hat{n}_x)/\rho_t \\ vq_t(\rho_s^+|_{\partial\Omega_E} - \rho_s^-|_{\partial\Omega_N}) \Psi_{\partial\Omega_N}^{(q_t)} H(v\hat{n}_y)/\rho_t \end{pmatrix} - \begin{pmatrix} vq_t(\rho_e^+|_{\partial\Omega_N} - \rho_e^-|_{\partial\Omega_E}) \Psi_{\partial\Omega_N}^{(q_t)} H(-v\hat{n}_x)/\rho_t \\ vq_t(\rho_s^+|_{\partial\Omega_N} - \rho_s^-|_{\partial\Omega_E}) \Psi_{\partial\Omega_N}^{(q_t)} H(-v\hat{n}_y)/\rho_t \end{pmatrix} \quad (\text{A.12})$$

The weak form of the third and fourth terms on the right-hand side of equation (13) is given by:

$$-\sum_F \int_{\partial\Omega_F} \frac{\rho_t}{2} \begin{pmatrix} \partial v / \partial x \\ \partial v / \partial y \end{pmatrix} \cdot \hat{\mathbf{n}} \Psi^{(q_t)} dS + \sum_E \int_{\Omega_E} \frac{\rho_t}{2} \begin{pmatrix} \partial v / \partial x \\ \partial v / \partial y \end{pmatrix} \cdot \nabla \Psi^{(q_t)} dV \quad (\text{A.13})$$

The flux term is defined as:

$$-\int_{\partial\Omega_F} \frac{\rho_t}{2} \begin{pmatrix} \partial v / \partial x \\ \partial v / \partial y \end{pmatrix} \cdot \hat{\mathbf{n}} \Psi^{(q_t)} dS = -\mathbf{F}_{\partial\Omega_F}^{(q_t,2)} \cdot \hat{\mathbf{n}} = -\mathbf{F}_{\partial\Omega_E}^{(q_t,2)} \cdot \hat{\mathbf{n}} - \mathbf{F}_{\partial\Omega_N}^{(q_t,2)} \cdot \hat{\mathbf{n}}. \quad (\text{A.14})$$

$$\mathbf{F}_{\partial\Omega_E}^{(q_t,2)} = \begin{pmatrix} \rho_t|_{\partial\Omega_E} (\partial v / \partial x)|_{\partial\Omega_E} \Psi_{\partial\Omega_E}^{(q_t)} H(v\hat{n}_x)/2 \\ \rho_t|_{\partial\Omega_E} (\partial v / \partial y)|_{\partial\Omega_E} \Psi_{\partial\Omega_E}^{(q_t)} H(v\hat{n}_y)/2 \end{pmatrix} - \begin{pmatrix} \rho_t|_{\partial\Omega_N} (\partial v / \partial x)|_{\partial\Omega_N} \Psi_{\partial\Omega_E}^{(q_t)} H(-v\hat{n}_x)/2 \\ \rho_t|_{\partial\Omega_N} (\partial v / \partial y)|_{\partial\Omega_N} \Psi_{\partial\Omega_E}^{(q_t)} H(-v\hat{n}_y)/2 \end{pmatrix} \quad (\text{A.15})$$

$$\mathbf{F}_{\partial\Omega_N}^{(q_t,2)} = -\begin{pmatrix} \rho_t|_{\partial\Omega_E} (\partial v / \partial x)|_{\partial\Omega_E} \Psi_{\partial\Omega_N}^{(q_t)} H(v\hat{n}_x)/2 \\ \rho_t|_{\partial\Omega_E} (\partial v / \partial y)|_{\partial\Omega_E} \Psi_{\partial\Omega_N}^{(q_t)} H(v\hat{n}_y)/2 \end{pmatrix} + \begin{pmatrix} \rho_t|_{\partial\Omega_N} (\partial v / \partial x)|_{\partial\Omega_N} \Psi_{\partial\Omega_N}^{(q_t)} H(-v\hat{n}_x)/2 \\ \rho_t|_{\partial\Omega_N} (\partial v / \partial y)|_{\partial\Omega_N} \Psi_{\partial\Omega_N}^{(q_t)} H(-v\hat{n}_y)/2 \end{pmatrix} \quad (\text{A.16})$$

The weak form of the fifth and sixth terms on the right-hand side of equation (13) can be written as:

$$\begin{aligned} & - \sum_F \int_{\partial\Omega_F} \left( \frac{(\rho_s^2 - \rho_e^2)}{2\sqrt{\rho_e^2 + \rho_s^2}} \frac{\partial v}{\partial x} - \frac{\rho_e \rho_s}{\sqrt{\rho_e^2 + \rho_s^2}} \frac{\partial v}{\partial y} \right) \cdot \hat{\mathbf{n}} \Psi^{(q_t)} dS \\ & + \sum_E \int_{\Omega_E} \left( \frac{(\rho_s^2 - \rho_e^2)}{2\sqrt{\rho_e^2 + \rho_s^2}} \frac{\partial v}{\partial x} - \frac{\rho_e \rho_s}{\sqrt{\rho_e^2 + \rho_s^2}} \frac{\partial v}{\partial y} \right) \cdot \nabla \Psi^{(q_t)} dV \end{aligned} \quad (\text{A.17})$$

The flux term is defined as:

$$- \int_{\partial\Omega_F} \left( \frac{(\rho_s^2 - \rho_e^2)}{2\sqrt{\rho_e^2 + \rho_s^2}} \frac{\partial v}{\partial x} - \frac{\rho_e \rho_s}{\sqrt{\rho_e^2 + \rho_s^2}} \frac{\partial v}{\partial y} \right) \cdot \hat{\mathbf{n}} \Psi^{(q_t)} dS = -\mathbf{F}_{\partial\Omega_F}^{(q_t,3)} \cdot \hat{\mathbf{n}} = -\mathbf{F}_{\partial\Omega_E}^{(q_t,3)} \cdot \hat{\mathbf{n}} - \mathbf{F}_{\partial\Omega_N}^{(q_t,3)} \cdot \hat{\mathbf{n}}. \quad (\text{A.18})$$

$$\begin{aligned} \mathbf{F}_{\partial\Omega_E}^{(q_t,3)} &= \left( \begin{array}{l} \left( \frac{(\rho_s^2|_{\partial\Omega_E} - \rho_e^2|_{\partial\Omega_E})}{2\sqrt{\rho_e^2|_{\partial\Omega_E} + \rho_s^2|_{\partial\Omega_E}}} \frac{\partial v}{\partial x}|_{\partial\Omega_E} - \frac{\rho_e|_{\partial\Omega_E} \rho_s|_{\partial\Omega_E}}{\sqrt{\rho_e^2|_{\partial\Omega_E} + \rho_s^2|_{\partial\Omega_E}}} \frac{\partial v}{\partial y}|_{\partial\Omega_E} \right) \Psi_{\partial\Omega_E}^{(q_t)} H(v\hat{n}_x) \\ \left( -\frac{\rho_e|_{\partial\Omega_E} \rho_s|_{\partial\Omega_E}}{\sqrt{\rho_e^2|_{\partial\Omega_E} + \rho_s^2|_{\partial\Omega_E}}} \frac{\partial v}{\partial x}|_{\partial\Omega_E} + \frac{(\rho_e^2|_{\partial\Omega_E} - \rho_s^2|_{\partial\Omega_E})}{2\sqrt{\rho_e^2|_{\partial\Omega_E} + \rho_s^2|_{\partial\Omega_E}}} \frac{\partial v}{\partial y}|_{\partial\Omega_E} \right) \Psi_{\partial\Omega_E}^{(q_t)} H(v\hat{n}_y) \end{array} \right) \\ & - \left( \begin{array}{l} \left( \frac{(\rho_s^2|_{\partial\Omega_N} - \rho_e^2|_{\partial\Omega_N})}{2\sqrt{\rho_e^2|_{\partial\Omega_N} + \rho_s^2|_{\partial\Omega_N}}} \frac{\partial v}{\partial x}|_{\partial\Omega_N} - \frac{\rho_e|_{\partial\Omega_N} \rho_s|_{\partial\Omega_N}}{\sqrt{\rho_e^2|_{\partial\Omega_N} + \rho_s^2|_{\partial\Omega_N}}} \frac{\partial v}{\partial y}|_{\partial\Omega_N} \right) \Psi_{\partial\Omega_N}^{(q_t)} H(-v\hat{n}_x) \\ \left( -\frac{\rho_e|_{\partial\Omega_N} \rho_s|_{\partial\Omega_N}}{\sqrt{\rho_e^2|_{\partial\Omega_N} + \rho_s^2|_{\partial\Omega_N}}} \frac{\partial v}{\partial x}|_{\partial\Omega_N} + \frac{(\rho_e^2|_{\partial\Omega_N} - \rho_s^2|_{\partial\Omega_N})}{2\sqrt{\rho_e^2|_{\partial\Omega_N} + \rho_s^2|_{\partial\Omega_N}}} \frac{\partial v}{\partial y}|_{\partial\Omega_N} \right) \Psi_{\partial\Omega_N}^{(q_t)} H(-v\hat{n}_y) \end{array} \right) \end{aligned} \quad (\text{A.19})$$

$$\begin{aligned} \mathbf{F}_{\partial\Omega_N}^{(q_t,3)} &= - \left( \begin{array}{l} \left( \frac{(\rho_s^2|_{\partial\Omega_E} - \rho_e^2|_{\partial\Omega_E})}{2\sqrt{\rho_e^2|_{\partial\Omega_E} + \rho_s^2|_{\partial\Omega_E}}} \frac{\partial v}{\partial x}|_{\partial\Omega_E} - \frac{\rho_e|_{\partial\Omega_E} \rho_s|_{\partial\Omega_E}}{\sqrt{\rho_e^2|_{\partial\Omega_E} + \rho_s^2|_{\partial\Omega_E}}} \frac{\partial v}{\partial y}|_{\partial\Omega_E} \right) \Psi_{\partial\Omega_N}^{(q_t)} H(v\hat{n}_x) \\ \left( -\frac{\rho_e|_{\partial\Omega_E} \rho_s|_{\partial\Omega_E}}{\sqrt{\rho_e^2|_{\partial\Omega_E} + \rho_s^2|_{\partial\Omega_E}}} \frac{\partial v}{\partial x}|_{\partial\Omega_E} + \frac{(\rho_e^2|_{\partial\Omega_E} - \rho_s^2|_{\partial\Omega_E})}{2\sqrt{\rho_e^2|_{\partial\Omega_E} + \rho_s^2|_{\partial\Omega_E}}} \frac{\partial v}{\partial y}|_{\partial\Omega_E} \right) \Psi_{\partial\Omega_N}^{(q_t)} H(v\hat{n}_y) \end{array} \right) \\ & + \left( \begin{array}{l} \left( \frac{(\rho_s^2|_{\partial\Omega_N} - \rho_e^2|_{\partial\Omega_N})}{2\sqrt{\rho_e^2|_{\partial\Omega_N} + \rho_s^2|_{\partial\Omega_N}}} \frac{\partial v}{\partial x}|_{\partial\Omega_N} - \frac{\rho_e|_{\partial\Omega_N} \rho_s|_{\partial\Omega_N}}{\sqrt{\rho_e^2|_{\partial\Omega_N} + \rho_s^2|_{\partial\Omega_N}}} \frac{\partial v}{\partial y}|_{\partial\Omega_N} \right) \Psi_{\partial\Omega_N}^{(q_t)} H(-v\hat{n}_x) \\ \left( -\frac{\rho_e|_{\partial\Omega_N} \rho_s|_{\partial\Omega_N}}{\sqrt{\rho_e^2|_{\partial\Omega_N} + \rho_s^2|_{\partial\Omega_N}}} \frac{\partial v}{\partial x}|_{\partial\Omega_N} + \frac{(\rho_e^2|_{\partial\Omega_N} - \rho_s^2|_{\partial\Omega_N})}{2\sqrt{\rho_e^2|_{\partial\Omega_N} + \rho_s^2|_{\partial\Omega_N}}} \frac{\partial v}{\partial y}|_{\partial\Omega_N} \right) \Psi_{\partial\Omega_N}^{(q_t)} H(-v\hat{n}_y) \end{array} \right) \end{aligned} \quad (\text{A.20})$$

## Appendix B. Dislocation loop test case

The test cases are carried out to demonstrate that the dislocation lines move correctly under given shear load. The dimensions of the simulation domain are  $40 \mu\text{m} \times 40 \mu\text{m} \times 2 \mu\text{m}$ . A structured mesh of first-order hexahedral cubic elements is used, which has an

element size of  $0.4 \mu\text{m}$ . A loading along  $+x$  or  $-x$  direction is applied on the top surface of the model, while the bottom surface of the plate is fixed, to induce a pure shear load. We prescribe different initial dislocation distributions in order to evaluate the dislocation line motion (as reported in Section 2.3) and dislocation curvature evolution respectively.

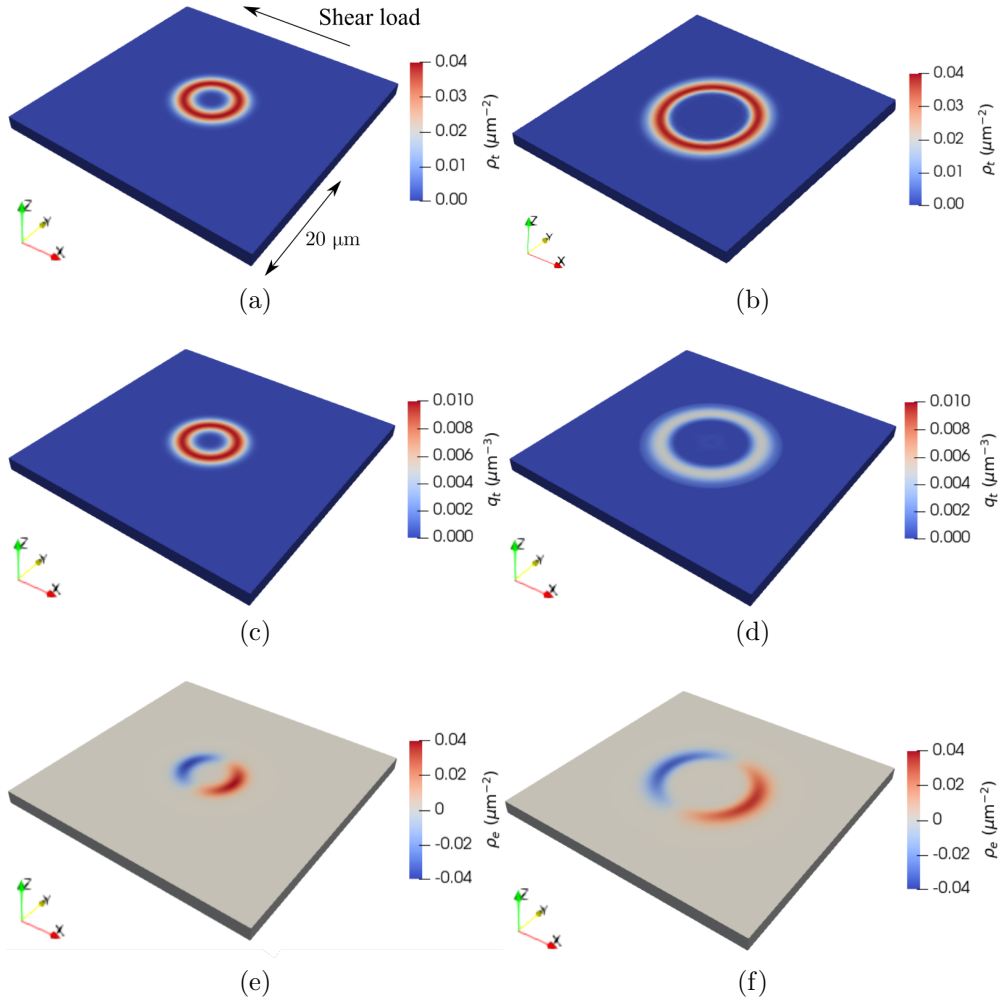


Figure B.17: Test case with dislocation loop: dislocation density at (a)  $t = 0$  and (b)  $t = 100 \mu\text{s}$ , curvature density at (c)  $t = 0$  and (d)  $t = 100 \mu\text{s}$ , edge GND density  $\rho_e$  at (e)  $t = 0$  and (f)  $t = 100 \mu\text{s}$ .

As shown in Fig. B.17, the dynamics of an expanding dislocation loop under shear load is modeled to test the curvature evolution using first-order shape functions. By initializing the CDD model variables using equations (C.1)-(C.3), one dislocation loop is initially set at the center of the simulation domain. It can be clearly observed that the dislocation loop expands under shear strain from Fig. B.17(a) to (b), while  $\rho_t$  remains the Gaussian distribution along the radial direction. The dislocation curvature  $q_t$  decreases during loop expansion, as shown in Fig. B.17(c)-(d), because the curvature is inversely proportional to the radius of the loop. The evolution of the edge GND density field  $\rho_e$  in the dislocation

loop is shown in Fig. B.17(e)-(f). The positive part moves along the positive  $x$  direction, while the negative part moves along the negative  $x$  direction. This test case indicates that the evolutions of dislocation density and curvature are identical to the analytical solutions and verifies the correctness of the implementation of the CDD equations in Section 2.

## Appendix C. Method of initial dislocation loops distribution

Given the center of the dislocation loop in the slip plane at coordinates  $(x_c, y_c)$ , a dislocation loop density  $\rho_{\max}$  and loop radius  $r$ , the dislocation density at coordinates  $(x, y)$  in the slip plane is given by:

$$\rho_t(x, y) = \frac{\rho_{\max}}{\sqrt{2\pi}w} \exp\left(-\frac{(R - |r|)^2}{2w^2}\right), \quad (\text{C.1})$$

where  $R = \sqrt{(x - x_c)^2 + (y - y_c)^2}$  is the distance from the center of the loop and  $w$  is the characteristic width of the dislocation density distribution. The distribution is considered uniform in  $z$ . A corresponding curvature density is obtained by  $q_t(x, y) = \rho_t(x, y)/r$ , and the edge and screw GND densities are given by:

$$\rho_e(x, y) = \frac{(x - x_c)}{R} \frac{\rho_{\max}}{\sqrt{2\pi}w} \exp\left(-\frac{(R - |r|)^2}{2w^2}\right) \text{sign}(r), \quad (\text{C.2})$$

$$\rho_s(x, y) = \frac{(y - y_c)}{R} \frac{\rho_{\max}}{\sqrt{2\pi}w} \exp\left(-\frac{(R - |r|)^2}{2w^2}\right) \text{sign}(r). \quad (\text{C.3})$$

Note that the radius  $r$  can be both positive or negative, representing a dislocation loop that expands or contracts under positive or negative resolved shear stress respectively.

## References

- [1] D. Hull, D. J. Bacon, *Introduction to dislocations*, Butterworth-Heinemann, 2001.
- [2] K. Lu, L. Lu, S. Suresh, *Strengthening materials by engineering coherent internal boundaries at the nanoscale*, Science 324 (5925) (2009) 349–352. doi:[10.1126/science.1159610](https://doi.org/10.1126/science.1159610)  
URL <https://www.science.org/doi/abs/10.1126/science.1159610>
- [3] B. He, B. Hu, H. Yen, G. Cheng, Z. Wang, H. Luo, M. Huang, High dislocation density-induced large ductility in deformed and partitioned steels, Science 357 (6355) (2017) 1029–1032. doi:[10.1126/science.aan0177](https://doi.org/10.1126/science.aan0177).
- [4] A. Irastorza-Landa, H. Van Swygenhoven, S. Van Petegem, N. Grilli, A. Bollhalder, S. Brandstetter, D. Grolimund, *Following dislocation patterning during fatigue*, Acta Materialia 112 (2016) 184–193. doi:<https://doi.org/10.1016/j.actamat.2016.04.011>  
URL <https://www.sciencedirect.com/science/article/pii/S1359645416302671>
- [5] S.-H. Kim, H. Kim, N. J. Kim, Brittle intermetallic compound makes ultrastrong low-density steel with large ductility, Nature 518 (7537) (2015) 77–79.
- [6] H. Wang, Z. Zhu, H. Chen, A. Wang, J. Liu, H. Liu, R. Zheng, S. Nai, S. Primig, S. Babu, et al., Effect of cyclic rapid thermal loadings on the microstructural evolution of a CrMnFeCoNi high-entropy alloy manufactured by selective laser melting, Acta Materialia 196 (2020) 609–625. doi:<https://doi.org/10.1016/j.actamat.2020.07.006>  
URL <https://www.sciencedirect.com/science/article/pii/S1359645420305048>

- [7] Y. M. Wang, T. Voisin, J. T. McKeown, J. Ye, N. P. Calta, Z. Li, Z. Zeng, Y. Zhang, W. Chen, T. T. Roehling, et al., Additively manufactured hierarchical stainless steels with high strength and ductility, *Nature materials* 17 (1) (2018) 63–71. [doi:  
https://doi.org/10.1038/nmat5021](https://doi.org/10.1038/nmat5021).
- [8] D. Herzog, V. Seyda, E. Wycisk, C. Emmelmann, *Additive manufacturing of metals*, *Acta Materialia* 117 (2016) 371–392. [doi:  
https://doi.org/10.1016/j.actamat.2016.07.019](https://doi.org/10.1016/j.actamat.2016.07.019).  
URL <https://www.sciencedirect.com/science/article/pii/S1359645416305158>
- [9] L. Aucott, H. Dong, W. Mirihanage, R. Atwood, A. Kidess, S. Gao, S. Wen, J. Marsden, S. Feng, M. Tong, et al., Revealing internal flow behaviour in arc welding and additive manufacturing of metals, *Nature communications* 9 (1) (2018) 1–7. [doi:  
https://doi.org/10.1038/s41467-018-07900-9](https://doi.org/10.1038/s41467-018-07900-9).
- [10] L. Thijss, K. Kempen, J.-P. Kruth, J. Van Humbeeck, *Fine-structured aluminium products with controllable texture by selective laser melting of pre-alloyed alsi10mg powder*, *Acta Materialia* 61 (5) (2013) 1809–1819. [doi:  
https://doi.org/10.1016/j.actamat.2012.11.052](https://doi.org/10.1016/j.actamat.2012.11.052).  
URL <https://www.sciencedirect.com/science/article/pii/S1359645412008592>
- [11] F. Yan, G. Liu, N. Tao, K. Lu, *Strength and ductility of 316l austenitic stainless steel strengthened by nano-scale twin bundles*, *Acta Materialia* 60 (3) (2012) 1059–1071. [doi:  
https://doi.org/10.1016/j.actamat.2011.11.009](https://doi.org/10.1016/j.actamat.2011.11.009).  
URL <https://www.sciencedirect.com/science/article/pii/S1359645411007956>
- [12] M. Shamsujjoha, S. R. Agnew, J. M. Fitz-Gerald, W. R. Moore, T. A. Newman, High strength and ductility of additively manufactured 316l stainless steel explained, *Metallurgical and Materials Transactions A* 49 (7) (2018) 3011–3027. [doi:  
https://doi.org/10.1007/s11661-018-4607-2](https://doi.org/10.1007/s11661-018-4607-2).
- [13] W. Xu, M. Brandt, S. Sun, J. Elambasseril, Q. Liu, K. Latham, K. Xia, M. Qian, *Additive manufacturing of strong and ductile ti–6al–4v by selective laser melting via in situ martensite decomposition*, *Acta Materialia* 85 (2015) 74–84. [doi:  
https://doi.org/10.1016/j.actamat.2014.11.028](https://doi.org/10.1016/j.actamat.2014.11.028).  
URL <https://www.sciencedirect.com/science/article/pii/S1359645414008817>
- [14] Z. Li, Y. Cui, W. Yan, D. Zhang, Y. Fang, Y. Chen, Q. Yu, G. Wang, H. Ouyang, C. Fan, et al., *Enhanced strengthening and hardening via self-stabilized dislocation network in additively manufactured metals*, *Materials Today* (2021). [doi:  
https://doi.org/10.1016/j.mattod.2021.06.002](https://doi.org/10.1016/j.mattod.2021.06.002).  
URL <https://www.sciencedirect.com/science/article/pii/S1369702121002054>
- [15] L. Liu, Q. Ding, Y. Zhong, J. Zou, J. Wu, Y.-L. Chiu, J. Li, Z. Zhang, Q. Yu, Z. Shen, *Dislocation network in additive manufactured steel breaks strength–ductility trade-off*, *Materials Today* 21 (4) (2018) 354–361. [doi:  
https://doi.org/10.1016/j.mattod.2017.11.004](https://doi.org/10.1016/j.mattod.2017.11.004).  
URL <https://www.sciencedirect.com/science/article/pii/S1369702117304625>
- [16] M. Pham, B. Dovgyy, P. Hooper, *Twinning induced plasticity in austenitic stainless steel 316l made by additive manufacturing*, *Materials Science and Engineering: A* 704 (2017) 102–111. [doi:  
https://doi.org/10.1016/j.msea.2017.07.082](https://doi.org/10.1016/j.msea.2017.07.082).  
URL <https://www.sciencedirect.com/science/article/pii/S0921509317309899>
- [17] D. Kong, C. Dong, S. Wei, X. Ni, L. Zhang, R. Li, L. Wang, C. Man, X. Li, *About metastable cellular structure in additively manufactured austenitic stainless steels*, *Additive Manufacturing* 38 (2021) 101804. [doi:  
https://doi.org/10.1016/j.addma.2020.101804](https://doi.org/10.1016/j.addma.2020.101804).  
URL <https://www.sciencedirect.com/science/article/pii/S2214860420311763>
- [18] G. Wang, H. Ouyang, C. Fan, Q. Guo, Z. Li, W. Yan, Z. Li, The origin of high-density dislocations in additively manufactured metals, *Materials Research Letters* 8 (8) (2020) 283–290. [doi:  
10.1080/21663831.2020.1751739](https://doi.org/10.1080/21663831.2020.1751739).
- [19] K. Bertsch, G. M. de Bellefon, B. Kuehl, D. Thoma, *Origin of dislocation structures in an additively manufactured austenitic stainless steel 316l*, *Acta Materialia* 199 (2020) 19–33. [doi:  
https://doi.org/10.1016/j.actamat.2020.07.063](https://doi.org/10.1016/j.actamat.2020.07.063).  
URL <https://www.sciencedirect.com/science/article/pii/S1359645420305796>
- [20] H. Mughrabi, *Dislocation clustering and long-range internal stresses in monotonically and cyclically deformed metal crystals*, *Rev. Phys. Appl.* 23 (4) (1988) 367–379. [doi:  
10.1051/rphysap:01988002304036700](https://doi.org/10.1051/rphysap:01988002304036700).  
URL [https://rphysap.journaldephysique.org/articles/rphysap/pdf/1988/04/rphysap\\_1988\\_](https://rphysap.journaldephysique.org/articles/rphysap/pdf/1988/04/rphysap_1988_)

- \_23\_4\_367\_0.pdf
- [21] J. Kratochvíl, R. Sedláček, Pattern formation in the framework of the continuum theory of dislocations, Phys. Rev. B 67 (2003) 094105. doi:[10.1103/PhysRevB.67.094105](https://doi.org/10.1103/PhysRevB.67.094105).  
URL <https://link.aps.org/doi/10.1103/PhysRevB.67.094105>
- [22] A. Irastorza-Landa, N. Grilli, H. Van Swygenhoven, Laue micro-diffraction and crystal plasticity finite element simulations to reveal a vein structure in fatigued cu, Journal of the Mechanics and Physics of Solids 104 (2017) 157–171. doi:<https://doi.org/10.1016/j.jmps.2017.04.010>.  
URL <https://www.sciencedirect.com/science/article/pii/S0022509616304781>
- [23] A. Irastorza-Landa, N. Grilli, H. V. Swygenhoven, Effect of pre-existing immobile dislocations on the evolution of geometrically necessary dislocations during fatigue, Modelling and Simulation in Materials Science and Engineering 25 (5) (2017) 055010. doi:[10.1088/1361-651x/aa6e24](https://doi.org/10.1088/1361-651x/aa6e24).  
URL <https://doi.org/10.1088/1361-651x/aa6e24>
- [24] N. Grilli, K. G. Janssens, H. Van Swygenhoven, Crystal plasticity finite element modelling of low cycle fatigue in fcc metals, Journal of the Mechanics and Physics of Solids 84 (2015) 424–435. doi:<https://doi.org/10.1016/j.jmps.2015.08.007>.  
URL <https://www.sciencedirect.com/science/article/pii/S0022509615300727>
- [25] S. Xia, A. El-Azab, Computational modelling of mesoscale dislocation patterning and plastic deformation of single crystals, Modelling and Simulation in Materials Science and Engineering 23 (5) (2015) 055009. doi:[10.1088/0965-0393/23/5/055009](https://doi.org/10.1088/0965-0393/23/5/055009).
- [26] D. Hughes, N. Hansen, The microstructural origin of work hardening stages, Acta Materialia 148 (2018) 374–383. doi:<https://doi.org/10.1016/j.actamat.2018.02.002>.  
URL <https://www.sciencedirect.com/science/article/pii/S1359645418301034>
- [27] M. V. Upadhyay, On the thermo-mechanical theory of field dislocations in transient heterogeneous temperature fields, Journal of the Mechanics and Physics of Solids 145 (2020) 104150. doi:<https://doi.org/10.1016/j.jmps.2020.104150>.  
URL <https://www.sciencedirect.com/science/article/pii/S0022509620303835>
- [28] M. Sudmanns, A. J. Birnbaum, Y. Gu, A. P. Iliopoulos, P. G. Callahan, J. G. Michopoulos, J. A. El-Awady, The interplay of local chemistry and plasticity in controlling microstructure formation during laser powder bed fusion of metals, Additive Manufacturing 55 (2022) 102791.
- [29] G. Facheris, M.-S. Pham, K. Janssens, S. Holdsworth, Microscopic analysis of the influence of ratcheting on the evolution of dislocation structures observed in aisi 316l stainless steel during low cycle fatigue, Materials Science and Engineering: A 587 (2013) 1–11. doi:<https://doi.org/10.1016/j.msea.2013.08.041>.  
URL <https://www.sciencedirect.com/science/article/pii/S0921509313009283>
- [30] E. Demir, D. Raabe, N. Zaafarani, S. Zaefferer, Investigation of the indentation size effect through the measurement of the geometrically necessary dislocations beneath small indents of different depths using ebsd tomography, Acta Materialia 57 (2) (2009) 559–569. doi:<https://doi.org/10.1016/j.actamat.2008.09.039>.  
URL <https://www.sciencedirect.com/science/article/pii/S1359645408007003>
- [31] S. Hocine, H. Van Swygenhoven, S. Van Petegem, C. S. T. Chang, T. Maimaitiyili, G. Tinti, D. Ferreira Sanchez, D. Grolimund, N. Casati, Operando x-ray diffraction during laser 3d printing, Materials Today 34 (2020) 30–40. doi:<https://doi.org/10.1016/j.mattod.2019.10.001>.  
URL <https://www.sciencedirect.com/science/article/pii/S136970211930803X>
- [32] K. Yamanaka, A. Kuroda, M. Ito, M. Mori, H. Bian, T. Shobu, S. Sato, A. Chiba, Quantifying the dislocation structures of additively manufactured ti-6al-4v alloys using x-ray diffraction line profile analysis, Additive Manufacturing 37 (2021) 101678. doi:<https://doi.org/10.1016/j.addma.2020.101678>.  
URL <https://www.sciencedirect.com/science/article/pii/S2214860420310502>
- [33] M. Lindroos, T. Pinomaa, K. Ammar, A. Laukkanen, N. Provatas, S. Forest, Dislocation density in cellular rapid solidification using phase field modeling and crystal plasticity, International Journal of Plasticity 148 (2022) 103139. doi:<https://doi.org/10.1016/j.ijplas.2021.103139>.

- URL <https://www.sciencedirect.com/science/article/pii/S0749641921002072>
- [34] R. LeSar, Simulations of dislocation structure and response, *Annu. Rev. Condens. Matter Phys.* 5 (1) (2014) 375–407. [doi:10.1146/annurev-conmatphys-031113-133858](https://doi.org/10.1146/annurev-conmatphys-031113-133858).
- [35] N. Hansen, D. Kuhlmann-Wilsdorf, **Low energy dislocation structures due to unidirectional deformation at low temperatures**, *Materials Science and Engineering* 81 (1986) 141–161. [doi:\[https://doi.org/10.1016/0025-5416\\(86\\)90258-2\]\(https://doi.org/10.1016/0025-5416\(86\)90258-2\)](https://doi.org/10.1016/0025-5416(86)90258-2)  
 URL <https://www.sciencedirect.com/science/article/pii/0025541686902582>
- [36] I. Groma, **Link between the microscopic and mesoscopic length-scale description of the collective behavior of dislocations**, *Physical Review B* 56 (10) (1997) 5807. [doi:10.1103/PhysRevB.56.5807](https://doi.org/10.1103/PhysRevB.56.5807).  
 URL <https://link.aps.org/doi/10.1103/PhysRevB.56.5807>
- [37] S. Groh, H. Zbib, **Advances in discrete dislocations dynamics and multiscale modeling**, *Journal of Engineering Materials and Technology* 131 (4) (2009). [doi:10.1115/1.3183783](https://doi.org/10.1115/1.3183783).  
 URL <https://doi.org/10.1115/1.3183783>
- [38] R. S. Fertig, S. P. Baker, **Simulation of dislocations and strength in thin films: A review**, *Progress in Materials Science* 54 (6) (2009) 874–908. [doi:<https://doi.org/10.1016/j.pmatsci.2009.03.004>](https://doi.org/10.1016/j.pmatsci.2009.03.004)  
 URL <https://www.sciencedirect.com/science/article/pii/S0079642509000164>
- [39] A. Lehtinen, F. Granberg, L. Laurson, K. Nordlund, M. J. Alava, **Multiscale modeling of dislocation-precipitate interactions in fe: from molecular dynamics to discrete dislocations**, *Physical Review E* 93 (1) (2016) 013309. [doi:10.1103/PhysRevE.93.013309](https://doi.org/10.1103/PhysRevE.93.013309).  
 URL <https://link.aps.org/doi/10.1103/PhysRevE.93.013309>
- [40] K. Yashiro, F. Kurose, Y. Nakashima, K. Kubo, Y. Tomita, H. Zbib, **Discrete dislocation dynamics simulation of cutting of precipitate and interfacial dislocation network in ni-based superalloys**, *International Journal of Plasticity* 22 (4) (2006) 713–723. [doi:<https://doi.org/10.1016/j.ijplas.2005.05.004>](https://doi.org/10.1016/j.ijplas.2005.05.004)  
 URL <https://www.sciencedirect.com/science/article/pii/S0749641905000963>
- [41] Y. Cui, G. Po, P. Srivastava, K. Jiang, V. Gupta, N. Ghoniem, **The role of slow screw dislocations in controlling fast strain avalanche dynamics in body-centered cubic metals**, *International Journal of Plasticity* 124 (2020) 117–132. [doi:<https://doi.org/10.1016/j.ijplas.2019.08.008>](https://doi.org/10.1016/j.ijplas.2019.08.008)  
 URL <https://www.sciencedirect.com/science/article/pii/S0749641919302980>
- [42] L. Wagner, **A discontinuous galerkin method for continuum dislocation dynamics in a fully-coupled elastoplasticity model**, Ph.D. thesis, Karlsruher Institut für Technologie (KIT) (2019).
- [43] I. Groma, F. Csikor, M. Zaiser, **Spatial correlations and higher-order gradient terms in a continuum description of dislocation dynamics**, *Acta Materialia* 51 (5) (2003) 1271–1281. [doi:\[https://doi.org/10.1016/S1359-6454\\(02\\)00517-7\]\(https://doi.org/10.1016/S1359-6454\(02\)00517-7\)](https://doi.org/10.1016/S1359-6454(02)00517-7)  
 URL <https://www.sciencedirect.com/science/article/pii/S1359645402005177>
- [44] C. Reuber, P. Eisenlohr, F. Roters, D. Raabe, **Dislocation density distribution around an indent in single-crystalline nickel: Comparing nonlocal crystal plasticity finite-element predictions with experiments**, *Acta Materialia* 71 (2014) 333–348. [doi:<https://doi.org/10.1016/j.actamat.2014.03.012>](https://doi.org/10.1016/j.actamat.2014.03.012)  
 URL <https://www.sciencedirect.com/science/article/pii/S1359645414001591>
- [45] A. El-Azab, **Statistical mechanics treatment of the evolution of dislocation distributions in single crystals**, *Physical Review B* 61 (18) (2000) 11956. [doi:10.1103/PhysRevB.61.11956](https://doi.org/10.1103/PhysRevB.61.11956).  
 URL <https://link.aps.org/doi/10.1103/PhysRevB.61.11956>
- [46] A. Ngan, **Dislocation-density kinematics: a simple evolution equation for dislocation density involving movement and tilting of dislocations**, *MRS Communications* 7 (3) (2017) 583–590.
- [47] T. Hochrainer, M. Zaiser, P. Gumbsch, **A three-dimensional continuum theory of dislocation systems: kinematics and mean-field formulation**, *Philosophical Magazine* 87 (8-9) (2007) 1261–1282. [doi:10.1080/14786430600930218](https://doi.org/10.1080/14786430600930218).
- [48] T. Hochrainer, S. Sandfeld, M. Zaiser, P. Gumbsch, **Continuum dislocation dynamics: towards a physical theory of crystal plasticity**, *Journal of the Mechanics and Physics of Solids* 63 (2014) 167–178. [doi:<https://doi.org/10.1016/j.jmps.2013.09.012>](https://doi.org/10.1016/j.jmps.2013.09.012)  
 URL <https://www.sciencedirect.com/science/article/pii/S0022509613001877>
- [49] Y. Zhang, A. H. Ngan, **Dislocation-density dynamics for modeling the cores and peierls stress of curved**

- dislocations, International Journal of Plasticity 104 (2018) 1–22.
- [50] M. Sudmanns, M. Stricker, D. Weygand, T. Hochrainer, K. Schulz, Dislocation multiplication by cross-slip and glissile reaction in a dislocation based continuum formulation of crystal plasticity, Journal of the Mechanics and Physics of Solids 132 (2019) 103695. doi:<https://doi.org/10.1016/j.jmps.2019.103695>.  
URL <https://www.sciencedirect.com/science/article/pii/S0022509619306428>
- [51] P. Lin, V. Vivekanandan, B. Anglin, C. Geller, A. El-Azab, Incorporating point defect generation due to jog formation into the vector density-based continuum dislocation dynamics approach, Journal of the Mechanics and Physics of Solids 156 (2021) 104609.
- [52] K. Schulz, L. Wagner, C. Wieners, A mesoscale continuum approach of dislocation dynamics and the approximation by a runge-kutta discontinuous galerkin method, International Journal of Plasticity 120 (2019) 248–261. doi:<https://doi.org/10.1016/j.ijplas.2019.05.003>.  
URL <https://www.sciencedirect.com/science/article/pii/S0749641919301688>
- [53] S. Sandfeld, T. Hochrainer, M. Zaiser, P. Gumbsch, Continuum modeling of dislocation plasticity: Theory, numerical implementation, and validation by discrete dislocation simulations, Journal of Materials Research 26 (5) (2011) 623–632. doi:[10.1557/jmr.2010.92](https://doi.org/10.1557/jmr.2010.92).
- [54] S. Sandfeld, E. Thawinan, C. Wieners, A link between microstructure evolution and macroscopic response in elasto-plasticity: Formulation and numerical approximation of the higher-dimensional continuum dislocation dynamics theory, International Journal of Plasticity 72 (2015) 1–20. doi:<https://doi.org/10.1016/j.ijplas.2015.05.001>.  
URL <https://www.sciencedirect.com/science/article/pii/S0749641915000704>
- [55] S. Sandfeld, M. Zaiser, Pattern formation in a minimal model of continuum dislocation plasticity, Modelling and Simulation in Materials Science and Engineering 23 (6) (2015) 065005. doi:[10.1088/0965-0393/23/6/065005](https://doi.org/10.1088/0965-0393/23/6/065005).
- [56] N. Grilli, D. Hu, D. Yushu, F. Chen, W. Yan, Crystal plasticity model of residual stress in additive manufacturing using the element elimination and reactivation method, Computational Mechanics (2021) 1–21doi:[10.1007/s00466-021-02116-z](https://doi.org/10.1007/s00466-021-02116-z).
- [57] D. Hu, N. Grilli, L. Wang, M. Yang, W. Yan, Microscale residual stresses in additively manufactured stainless steel: Computational simulation, Journal of the Mechanics and Physics of Solids (2022) 104822doi:<https://doi.org/10.1016/j.jmps.2022.104822>.  
URL <https://www.sciencedirect.com/science/article/pii/S0022509622000394>
- [58] C. J. Permann, D. R. Gaston, D. Andrs, R. W. Carlsen, F. Kong, A. D. Lindsay, J. M. Miller, J. W. Peterson, A. E. Slaughter, R. H. Stogner, R. C. Martineau, Moose: Enabling massively parallel multiphysics simulation, SoftwareX 11 (2020) 100430. doi:<https://doi.org/10.1016/j.softx.2020.100430>.  
URL <https://www.sciencedirect.com/science/article/pii/S2352711019302973>
- [59] R. J. Asaro, J. Rice, Strain localization in ductile single crystals, Journal of the Mechanics and Physics of Solids 25 (5) (1977) 309–338. doi:[https://doi.org/10.1016/0022-5096\(77\)90001-1](https://doi.org/10.1016/0022-5096(77)90001-1).  
URL <https://www.sciencedirect.com/science/article/pii/0022509677900011>
- [60] S. R. Kalidindi, Incorporation of deformation twinning in crystal plasticity models, Journal of the Mechanics and Physics of Solids 46 (2) (1998) 267–290. doi:[https://doi.org/10.1016/S0022-5096\(97\)00051-3](https://doi.org/10.1016/S0022-5096(97)00051-3).  
URL <https://www.sciencedirect.com/science/article/pii/S0022509697000513>
- [61] L. Vujošević, V. Lubarda, Finite-strain thermoelasticity based on multiplicative decomposition of deformation gradient, Theoretical and applied mechanics (28-29) (2002) 379–399. doi:[10.2298/TAM0229379V](https://doi.org/10.2298/TAM0229379V).
- [62] F. Roters, P. Eisenlohr, L. Hantcherli, D. D. Tjahjanto, T. R. Bieler, D. Raabe, Overview of constitutive laws, kinematics, homogenization and multiscale methods in crystal plasticity finite-element modeling: Theory, experiments, applications, Acta Materialia 58 (4) (2010) 1152–1211. doi:<https://doi.org/10.1016/j.actamat.2009.10.058>.  
URL <https://www.sciencedirect.com/science/article/pii/S1359645409007617>

- [63] F. Roters, M. Diehl, P. Shanthraj, P. Eisenlohr, C. Reuber, S. Wong, T. Maiti, A. Ebrahimi, T. Hochrainer, H.-O. Fabritius, S. Nikolov, M. Friák, N. Fujita, N. Grilli, K. Janssens, N. Jia, P. Kok, D. Ma, F. Meier, E. Werner, M. Stricker, D. Weygand, D. Raabe, *Damask – the Düsseldorf advanced material simulation kit for modeling multi-physics crystal plasticity, thermal, and damage phenomena from the single crystal up to the component scale*, Computational Materials Science 158 (2019) 420 – 478. doi:<https://doi.org/10.1016/j.commatsci.2018.04.030>  
URL <http://www.sciencedirect.com/science/article/pii/S0927025618302714>
- [64] Symposium on internal stresses in metals and alloys, Nature 164 (1949) 296–296. doi:[10.1038/164296a0](https://doi.org/10.1038/164296a0).  
URL <https://www.nature.com/articles/164296a0>
- [65] D. N. Blaschke, A. Hunter, D. L. Preston, *Analytic model of the remobilization of pinned glide dislocations: Including dislocation drag from phonon wind*, International Journal of Plasticity 131 (2020) 102750. doi:<https://doi.org/10.1016/j.ijplas.2020.102750>  
URL <https://www.sciencedirect.com/science/article/pii/S0749641919309258>
- [66] K. Chu, M. E. Foster, R. B. Sills, X. Zhou, T. Zhu, D. L. McDowell, Temperature and composition dependent screw dislocation mobility in austenitic stainless steels from large-scale molecular dynamics, npj Computational Materials 6 (1) (2020) 1–10.
- [67] M. Pham, S. Holdsworth, K. Janssens, E. Mazza, *Cyclic deformation response of aisi 316l at room temperature: mechanical behaviour, microstructural evolution, physically-based evolutionary constitutive modelling*, International Journal of Plasticity 47 (2013) 143–164. doi:<https://doi.org/10.1016/j.ijplas.2013.01.017>  
URL <https://www.sciencedirect.com/science/article/pii/S0749641913000272>
- [68] I. Groma, *Statistical theory of dislocation*, in: Z. H. Mesarovic S., Forest S. (Ed.), Mesoscale Models, Vol. 587, CISM International Centre for Mechanical Sciences (Courses and Lectures), Springer, Cham, 2019, pp. 87–139. doi:[https://doi.org/10.1007/978-3-319-94186-8\\_3](https://doi.org/10.1007/978-3-319-94186-8_3)  
URL [https://link.springer.com/chapter/10.1007/978-3-319-94186-8\\_3#citeas](https://link.springer.com/chapter/10.1007/978-3-319-94186-8_3#citeas)
- [69] A. Arsenlis, D. M. Parks, *Modeling the evolution of crystallographic dislocation density in crystal plasticity*, Journal of the Mechanics and Physics of Solids 50 (9) (2002) 1979–2009. doi:[https://doi.org/10.1016/S0022-5096\(01\)00134-X](https://doi.org/10.1016/S0022-5096(01)00134-X)  
URL <https://www.sciencedirect.com/science/article/pii/S002250960100134X>
- [70] N. Grilli, K. Janssens, J. Nellessen, S. Sandlöbes, D. Raabe, *Multiple slip dislocation patterning in a dislocation-based crystal plasticity finite element method*, International Journal of Plasticity 100 (2018) 104–121. doi:<https://doi.org/10.1016/j.ijplas.2017.09.015>  
URL <https://www.sciencedirect.com/science/article/pii/S0749641917305570>
- [71] M. Daymond, P. Bouchard, Elastoplastic deformation of 316 stainless steel under tensile loading at elevated temperatures, Metallurgical and Materials transactions A 37 (6) (2006) 1863–1873. doi:[10.1007/s11661-006-0129-4](https://doi.org/10.1007/s11661-006-0129-4).
- [72] W. Jiang, Y. Zhang, W. Woo, *Using heat sink technology to decrease residual stress in 316l stainless steel welding joint: Finite element simulation*, International journal of pressure vessels and piping 92 (2012) 56–62. doi:<https://doi.org/10.1016/j.ijpvp.2012.01.002>  
URL <https://www.sciencedirect.com/science/article/pii/S0308016112000038>
- [73] M. Calcagnotto, D. Ponge, E. Demir, D. Raabe, *Orientation gradients and geometrically necessary dislocations in ultrafine grained dual-phase steels studied by 2d and 3d ebsd*, Materials Science and Engineering: A 527 (10) (2010) 2738–2746. doi:<https://doi.org/10.1016/j.msea.2010.01.004>  
URL <https://www.sciencedirect.com/science/article/pii/S0921509310000195>
- [74] Y. Zhu, Y. Xiang, *A continuum model for dislocation dynamics in three dimensions using the dislocation density potential functions and its application to micro-pillars*, Journal of the Mechanics and Physics of Solids 84 (2015) 230–253.
- [75] T. Hochrainer, *Multipole expansion of continuum dislocations dynamics in terms of alignment tensors*, Philosophical Magazine 95 (12) (2015) 1321–1367. arXiv:<https://doi.org/10.1080/14786435.2015.1026297>, doi:[10.1080/14786435.2015.1026297](https://doi.org/10.1080/14786435.2015.1026297).

- URL <https://doi.org/10.1080/14786435.2015.1026297>
- [76] G. Edelin, On dislocation climb rate, *The Philosophical Magazine: A Journal of Theoretical Experimental and Applied Physics* 23 (186) (1971) 1547–1550. [doi:10.1080/14786437108217021](https://doi.org/10.1080/14786437108217021).
- [77] J.-S. Zhang, High temperature deformation and fracture of materials, Elsevier, 2010.
- [78] D. Graham, D. Tomlin, Self-diffusion in iron, *Philosophical Magazine* 8 (93) (1963) 1581–1585.
- [79] F. Roters, D. Raabe, G. Gottstein, *Work hardening in heterogeneous alloys—a microstructural approach based on three internal state variables*, *Acta materialia* 48 (17) (2000) 4181–4189. [doi:https://doi.org/10.1016/S1359-6454\(00\)00289-5](https://doi.org/10.1016/S1359-6454(00)00289-5).  
URL <https://www.sciencedirect.com/science/article/pii/S1359645400002895>
- [80] P. M. Anderson, J. P. Hirth, J. Lothe, Theory of dislocations, Cambridge University Press, 2017.
- [81] Z. Basinski, S. Basinski, *Fundamental aspects of low amplitude cyclic deformation in face-centred cubic crystals*, *Progress in Materials Science* 36 (1992) 89–148. [doi:https://doi.org/10.1016/0079-6425\(92\)90006-S](https://doi.org/10.1016/0079-6425(92)90006-S).  
URL <https://www.sciencedirect.com/science/article/pii/007964259290006S>
- [82] S. Catalao, X. Feaugas, P. Pilvin, M.-T. Cabrillat, *Dipole heights in cyclically deformed polycrystalline aisi 316l stainless steel*, *Materials Science and Engineering: A* 400-401 (2005) 349–352, dislocations 2004. [doi:https://doi.org/10.1016/j.msea.2005.03.094](https://doi.org/10.1016/j.msea.2005.03.094).  
URL <https://www.sciencedirect.com/science/article/pii/S0921509305003242>
- [83] N. Grilli, Physics-based constitutive modelling for crystal plasticity finite element computation of cyclic plasticity in fatigue, Tech. rep., EPFL (2016).
- [84] B. Clausen, T. Lorentzen, T. Leffers, Self-consistent modelling of the plastic deformation of F.C.C. polycrystals and its implications for diffraction measurements of internal stresses, *Acta Materialia* 46 (9) (1998) 3087–3098. [doi:10.1016/S1359-6454\(98\)00014-7](https://doi.org/10.1016/S1359-6454(98)00014-7).
- [85] W. Chen, T. Voisin, Y. Zhang, J.-B. Forien, C. M. Spadaccini, D. L. McDowell, T. Zhu, Y. M. Wang, Microscale residual stresses in additively manufactured stainless steel, *Nature communications* 10 (1) (2019) 1–12. [doi:10.1038/s41467-019-12265-8](https://doi.org/10.1038/s41467-019-12265-8).
- [86] L. Wang, Y. Zhang, W. Yan, *Evaporation model for keyhole dynamics during additive manufacturing of metal*, *Physical Review Applied* 14 (6) (2020) 064039. [doi:10.1103/PhysRevApplied.14.064039](https://doi.org/10.1103/PhysRevApplied.14.064039).  
URL <https://link.aps.org/doi/10.1103/PhysRevApplied.14.064039>
- [87] W. Yan, S. Lin, O. L. Kafka, Y. Lian, C. Yu, Z. Liu, J. Yan, S. Wolff, H. Wu, E. Ndip-Agbor, et al., Data-driven multi-scale multi-physics models to derive process–structure–property relationships for additive manufacturing, *Computational Mechanics* 61 (5) (2018) 521–541. [doi:10.1007/s00466-018-1539-z](https://doi.org/10.1007/s00466-018-1539-z).
- [88] M. Yang, L. Wang, W. Yan, Phase-field modeling of grain evolutions in additive manufacturing from nucleation, growth, to coarsening, *npj Computational Materials* 7 (1) (2021) 1–12. [doi:10.1038/s41524-021-00524-6](https://doi.org/10.1038/s41524-021-00524-6).
- [89] N. Grilli, M. Koslowski, *The effect of crystal orientation on shock loading of single crystal energetic materials*, *Computational Materials Science* 155 (2018) 235–245. [doi:https://doi.org/10.1016/j.commatsci.2018.08.059](https://doi.org/10.1016/j.commatsci.2018.08.059).  
URL <https://www.sciencedirect.com/science/article/pii/S0927025618305883>
- [90] N. Grilli, D. Hu, D. Yushu, F. Chen, W. Yan, Crystal plasticity model of residual stress in additive manufacturing using the element elimination and reactivation method, *Computational Mechanics* 69 (3) (2022) 825–845.
- [91] Wikipedia, *Euler angles — wikipedia, the free encyclopedia*, [Online; checked on 11 May 2021] (2021).  
URL [https://en.wikipedia.org/wiki/Euler\\_angles](https://en.wikipedia.org/wiki/Euler_angles)
- [92] N. Grilli, A. C. Cocks, E. Tarleton, *Crystal plasticity finite element modelling of coarse-grained  $\alpha$ -uranium*, *Computational Materials Science* 171 (2020) 109276. [doi:https://doi.org/10.1016/j.commatsci.2019.109276](https://doi.org/10.1016/j.commatsci.2019.109276).  
URL <https://www.sciencedirect.com/science/article/pii/S0927025619305750>
- [93] Z. Liu, D. Zhao, P. Wang, M. Yan, C. Yang, Z. Chen, J. Lu, Z. Lu, *Additive manufacturing of metals: Microstructure evolution and multistage control*, *Journal of Materials Science Technology* 100 (2022) 224–236. [doi:https://doi.org/10.1016/j.jmst.2021.06.011](https://doi.org/10.1016/j.jmst.2021.06.011).

- [94] N. Grilli, Physics-based constitutive modelling for crystal plasticity finite element computation of cyclic plasticity in fatigue, Ph.D. thesis, École Polytechnique Fédérale de Lausanne (2016). [doi:10.5075/epfl-thesis-7251](https://doi.org/10.5075/epfl-thesis-7251).  
URL <https://infoscience.epfl.ch/record/223625>
- [95] J. Li, M. Yi, H. Wu, Q. Fang, Y. Liu, B. Liu, K. Zhou, P. K. Liaw, Fine-grain-embedded dislocation-cell structures for high strength and ductility in additively manufactured steels, Materials Science and Engineering: A 790 (2020) 139736. [doi:https://doi.org/10.1016/j.msea.2020.139736](https://doi.org/10.1016/j.msea.2020.139736).  
URL <https://www.sciencedirect.com/science/article/pii/S092150932030811X>
- [96] A. J. Birnbaum, J. C. Steuben, E. J. Barrick, A. P. Iliopoulos, J. G. Michopoulos, Intrinsic strain aging, 3 boundaries, and origins of cellular substructure in additively manufactured 316l, Additive Manufacturing 29 (2019) 100784. [doi:https://doi.org/10.1016/j.addma.2019.100784](https://doi.org/10.1016/j.addma.2019.100784).  
URL <https://www.sciencedirect.com/science/article/pii/S2214860419303811>
- [97] M. He, H. Cao, Q. Liu, J. Yi, Y. Ni, S. Wang, Evolution of dislocation cellular pattern in inconel 718 alloy fabricated by laser powder-bed fusion, Additive Manufacturing 55 (2022) 102839. [doi:https://doi.org/10.1016/j.addma.2022.102839](https://doi.org/10.1016/j.addma.2022.102839).  
URL <https://www.sciencedirect.com/science/article/pii/S221486042200238X>